Insights into the mechanism of electrocatalytic CO2 reduction and concomitant catalyst degradation pathways

Raaijman, S.J.

A

Supporting information for Chapter 2: High-pressure CO electroreduction at silver produces ethanol and propanol

A.1. Supporting experimental

A.1.1. Chemicals

All solutions were prepared by dissolving appropriate amounts of chemicals, used as received unless otherwise indicated, in high purity Milli-Q water (Millipore, $18.2\ M\Omega \cdot cm$). All experiments were conducted in $300\ mL$ $0.5\ M$ KOH (99.95%, Alfa Aesar) electrolyte purged and pressurized with carbon monoxide (Linde, 4.7), whilst the counter electrode compartment was purged with nitrogen (Linde, 2.0).

A.1.2. Electrochemistry

Potentials were controlled via either a Solartron (Energylab XM with 2A booster) or Autolab (PGSTAT302N) potentiostat in a three-electrode configuration. Solution resistances were determined via impedance before the start of the experiment and at regular intervals during the measurement, but reported potential values are not corrected for ohmic drop. High-pressure electrochemical cell and product detection. A home-made three-compartment electrochemical cell designed to fit inside an autoclave (Premex, Hastelloy C22, 600 mL) was used for all experiments reported in this work (Figure A.1). The autoclave had a total of three gas inlets (CE compartment, WE compartment topside (not used) and WE backside) and two gas

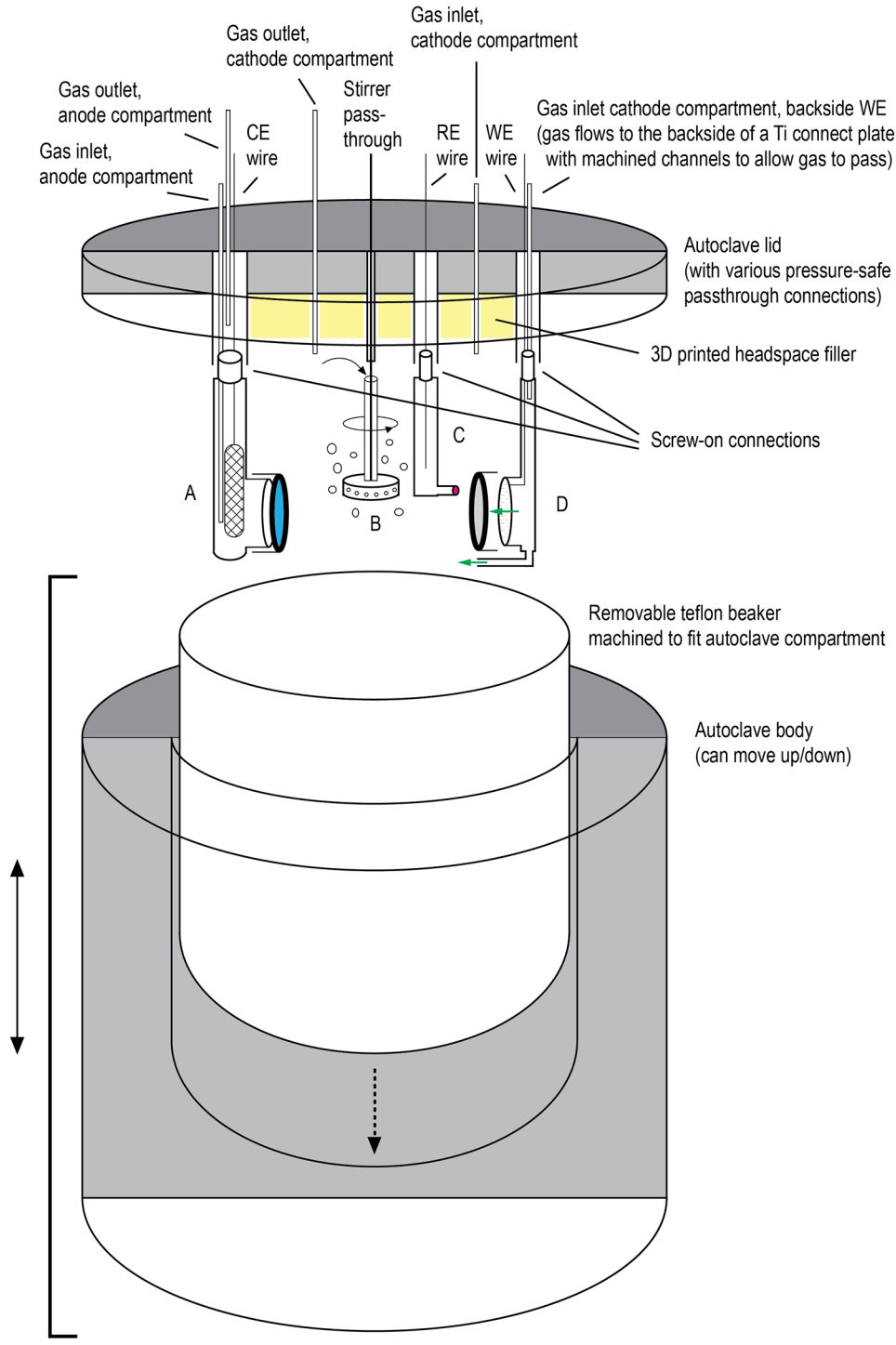

Figure A.1: Schematic of the high-pressure setup.

outlets (CE and WE compartment outlets). The inlets of the autoclave were attached to calibrated mass flow controllers (Brooks, Delta Smart II) connected to their respective gas bottles, whilst the outlet was attached to a back-pressure regulator (Equilibar) to regulate pressure inside the reaction chamber and allow for constant flow. Outflows of excess gases for counter and working compartments were united downstream, but the existence of a constant net positive flux for both compartments prevented mixing at points located upstream. After, exhaust gas was led through a dehumidifier (Perma Pure, MD-050-24S-2) prior to being introduced into a gas chromatograph (G.A.S, CompactGC 4.0).

The electrochemical cell was comprised of two sections: a bottom and a top half. The lower half contained the electrochemical cell and consisted of a cylindrical PTFE beaker that was machined to precisely fit the bottom of the autoclave. The top half of the cell was affixed to the top of the autoclave, and housed a series of machined plastic pieces that extended down into the PTFE beaker upon assembly. Specifically, the top contained a total of five elements: separate housings for both the counter (Figure A.1, A) and reference electrodes (Figure A.1, C), a machined component capable of flowing gases along the back of the working electrode into the reaction vessel (Figure A.1, D), a vertical stirring rod (Figure A.1, B), and a final piece of 3D printed solid plastic (3D printed with Form labs 2 SLA 3D printer using FLGPC02 resin) that was shaped so as to fill the empty spaces in-between the other components above the electrolyte level (Figure A.1, yellow sections). Electrical contact with the outside was established via pass-through Swagelok fittings located in the top of the autoclave.

The counter electrode (platinum mesh, 99.9%, Alfa Aesar) was housed in a rectangular enclosure made out of PEEK with an internal volume of ca. $20\ mL$. The anolyte was isolated from the rest of the cell via an anion exchange membrane (AEM, Fumasen, FAB-PK-130) of ca. $7\ cm^2$. The anolyte was constantly purged with nitrogen to facilitate mixing and the removal of bubbles, whilst also serving as an internal standard for gas quantification. The membrane separating the two compartments was replaced daily, or alternatively after each experiment (for experiments $> 12\ h$).

A home-made Ag/AgCl wire in contact with KCl solution made up the reference electrode. Prior to each experiment the AgCl layer was renewed by submerging the silver wire (99.9%, Alfa Aesar) in a $0.1\ M$ HCl solution (Ph. Eur., Merck) and applying a current of $+20\ mA$ for $20\ seconds$ vs. a Pt wire to form a silver chloride overlayer, which is the electrochemical equivalent of some commonly employed[1, 2] chemical treatments to generate a AgCl layer. Then, the wire was thoroughly rinsed with Milli-Q water, after which it was submerged in a machined Luggin capillary made from Kel-F containing ca. 10 mL AgCl saturated (0.16 M) 3 M KCl solution (Merck). The tip of the Luggin capillary was located in close proximity to the bottom-half of the working electrode surface (ca. $1\ mm$ away) and terminated with a PEEK frit with $2\ \mu m$ pores (Idex, A-710) to separate the working electrolyte from the reference solution. The working electrode assembly was comprised of an open-ended hollow rod that allowed for gases to be introduced to the reaction vessel. Electrical contact with the working electrode was established through the backside of the WE via a

circular titanium plate (connected to a lead) that had flow channels machined into it to allow gases to reach the backside of the electrode. However, no means of closing the lower end of the tube were present. Thus, gases could also flow past the backside of the electrode and out of the bottom tube into the electrolyte. A silver GDE (Dioxide Materials, Ag/ionomer coating on carbon paper) was cut to size and used as received, with a total geometric area of $1\ cm^2$ exposed to the electrolyte. The working electrode was replaced for each individual measurement.

A.1.3. IR drop determination

Solution resistances were determined at the start of each experiment via impedance spectroscopy near the open circuit potential and assumed to be equal to the measured real impedance at $10\ kHz$[3], which varied between 4.8 and $5.5\ \Omega$ for all experiments reported in this work. Potentials as we report them ($V\ vs.\ Ag|AgCl|KCl_{3\ M}$) can be converted to the reversible hydrogen electrode (RHE) scale via Equation A.1, and the ohmic resistance compensated to obtain the 'real' interfacial potential via Equation A.2 where conventional signage for cathodic (negative) and anodic (positive) current applies. Using a standard potential of $E^{3\ M\ Cl^-}_{Ag|AgCl} = +0.21\ V\ vs.\ SHE$, a pH of 13.7 for our $0.5\ M$ KOH electrolyte, an R value of $5\ \Omega$, and $-0.5\ A$ of current at the most negatively applied potential of $-4.5\ V$ (see Figure A.6, considering $1\ cm^2$ of area), we obtain a 'real' potential of ca. $-1\ V\ vs.\ RHE$.

$$V\ vs.\ RHE = V\ vs.\ Ag|AgCl|KCl_{3M} + E^{3\ M\ Cl^-}_{Ag|AgCl}(V) + pH * 59.1 * 10^{-3}(V) \quad \text{(A.1)}$$

$$V_{real} = V_{applied} - i(A) * R_u(\Omega) \quad \text{(A.2)}$$

A.1.4. Cleaning

Organic and metallic contaminants were removed from the cell body by submerging in acidified ($0.5\ M$ H_2SO_4, Ph. Eur, Merck) permanganate solution ($1\ g \cdot L^{-1}$ $KMnO_4$, Baker Chemicals) for a minimum of $12\ h$, which was rinsed with dilute piranha solution followed by thorough rinsing with Milli-Q water prior to use. The upper compartment housing the electrode compartments were cleaned by storing in Milli-Q water and rinsing them prior to use. All parts of the cell in direct contact with electrolyte were made of various chemically inert polymers (PTFE, PEEK or Kel-F), to prevent metal ion leaching by the highly alkaline electrolyte.

A.1.5. Product analysis

The gaseous cell exhaust was sampled at regular intervals ($1\ to\ 6\ times/hr$) via gas chromatography, with the sampling frequency depending on reactant gas inflow ($15-150\ mL_n \cdot min^{-1}$) with lower flows (and less frequent sampling intervals) being used for experiments that necessitated longer reaction times (i.e. lower currents). The addition of a known flow of inert gas (nitrogen) was used as an internal standard to calculate the flows of the individual components. After each experiment, a liquid sample was taken from the catholyte and analyzed via NMR with DMSO as an internal standard similar to the procedure as described by Kuhl et al.[3]

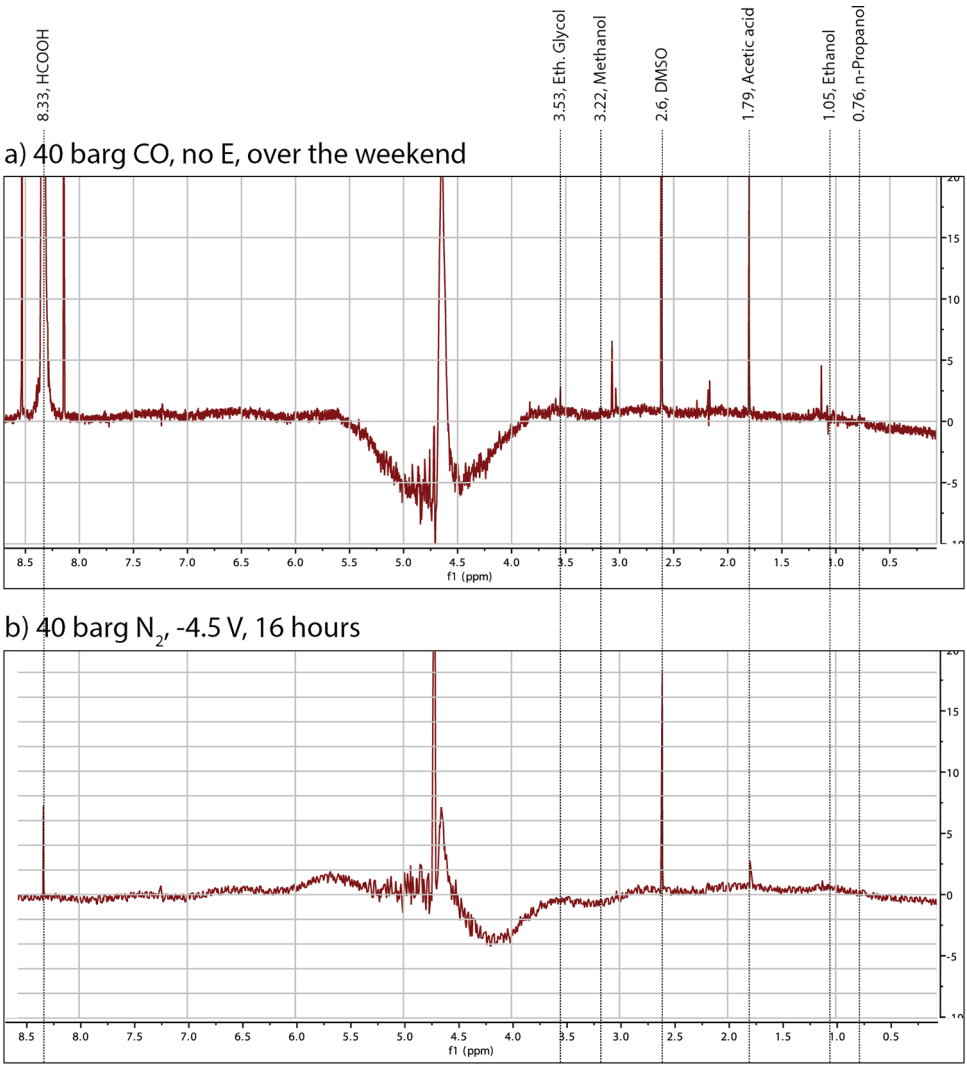

Figure A.2: NMR spectra control experiments.

A.2. Control experiments to verify product origin

Two measurements were performed so as to verify that the origin of products is electrochemical in nature, with the electrolyte composition investigated via NMR for products (Figure A.2). Firstly, the reactor was set up identically as discussed previously and pressurized to $40\ barg$ of CO, including continuous gas flow. However, no potential was applied to the WE. This condition was kept for $> 60\ hours$, and the 'electrolyte' was analyzed for products (Figure A.2a). In this instance, two liquid (and no gaseous) products discussed in the main text were observed: formic acid and acetic acid. Formic acid formation from CO + OH^- has been addressed in the

main text, but the fact that we see acetic acid is peculiar. Although its formation rate is much below what we observe in the presence of an applied potential (it is about 35% of the lowest formation rate detected in this work i.e., for $10\ barg$ of CO at $-2\ V$), one would not expect its formation at all in absence of an applied potential. This trace of acetic acid may originate from a reaction between CH_4 and CO_2.[4] Carbon dioxide will be present in minor quantities due to the reverse water-gas shift reaction ($CO + H_2O \rightleftharpoons CO_2 + H_2$), whilst methane is present as an impurity in the CO gas (and we also observe in the GC). Although this reaction is unfavorable, and the quantities of required reactants are low, it may serve as an explanation for the trace of acetic acid we observe, even in the absence of an applied potential.

As for the second control experiment, we applied $-4.5\ V$ under $40\ barg$ of N_2. In this instance, no appreciable quantities of any kind of product other than hydrogen were observed (although a small spike representing formic acid can be seen, likely originating from traces of CO left in the dead spots of the system as we also found from GC, but its concentration is insignificant).

A.3. Formation rates for non-CORR products

The observed formation rates for H_2 and HCOOH are depicted in Figure A.3.

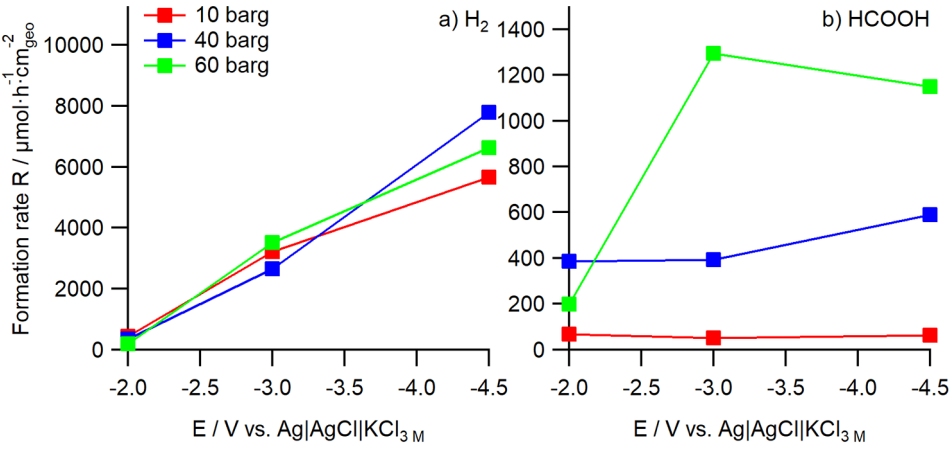

Figure A.3: Area-normalized formation rates for non-CORR products.

A.4. Electrochemical response of the system

Partial current densities for the CORR-related products discussed in the main text are depicted in Figure A.4, and the partial current density for hydrogen is shown in Figure A.5. Beware of the difference in scale between the two figures (μA vs mA for Figures A.4 and A.5, respectively). Total system current densities for the various investigated conditions are depicted in Figure A.6.

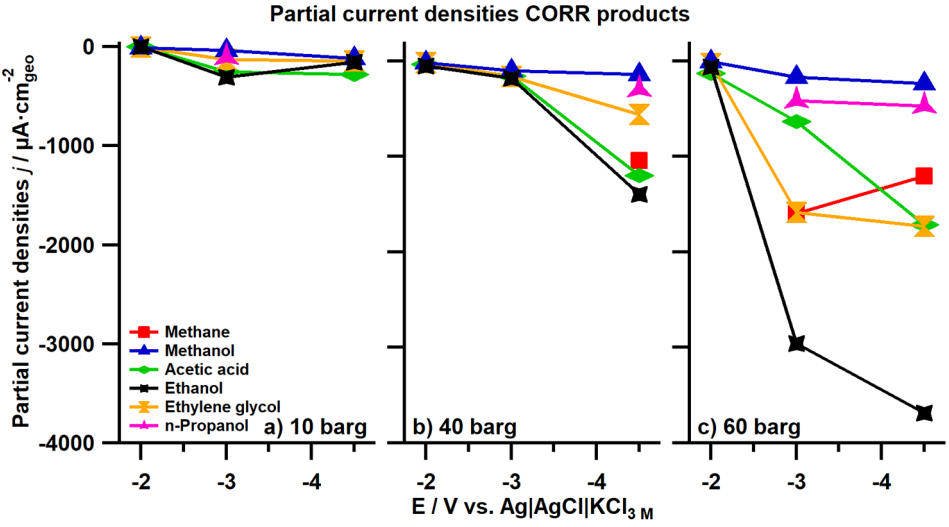

Figure A.4: Partial-current density equivalent plot of Figure 2.1 in the main text.

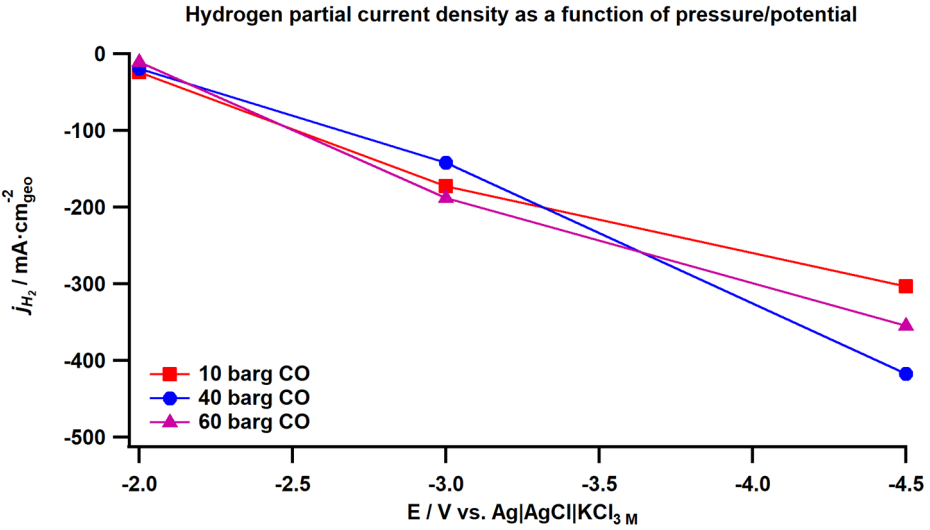

Figure A.5: Pressure-dependent partial current density of hydrogen.

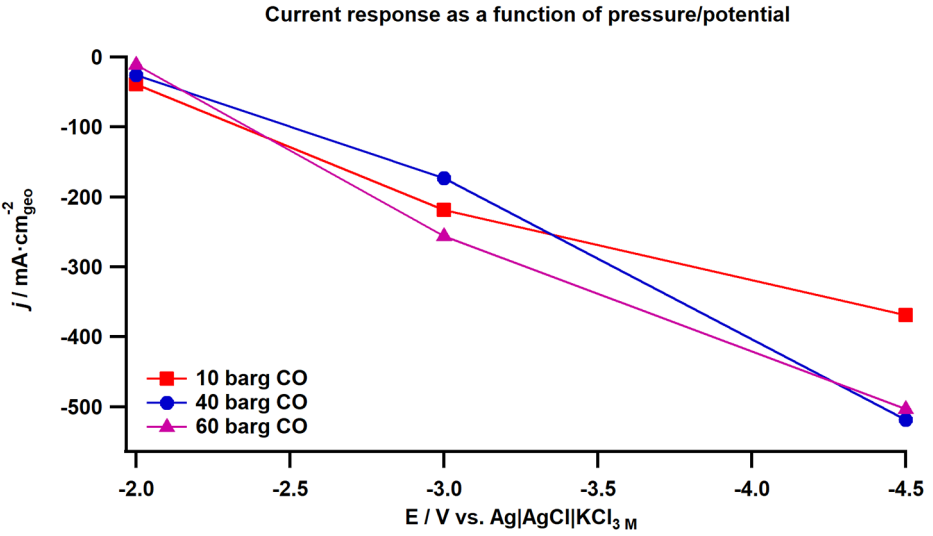

Figure A.6: Total current densities for the various investigated conditions.

Faradaic efficiencies for the measurements discussed in the main text are provided in Table A.1. Two main points stand out. Firstly, CORR products are the minority species, which is reflected in low faradaic efficiency values for these products. Secondly, not all current in the system is accounted for. The latter we explain by the fact that our reactor at the time of measuring did not have a perfect seal (an issue that has since been addressed), allowing part of the hydrogen to escape the system. Considering that hydrogen accounts for the vast majority of the current, a loss of hydrogen (as it is very fugacious) through to a small leak in the system has large repercussions for the total faradaic efficiency. However, this issue is expected to have little to no influence on the identities and quantities of solution-phase products, as they are not meaningfully present in the gas phase due to their lower vapor pressure, and therefore should not significantly influence our discussion. Regarding methane, which would be affected, it is only sporadically observed (to rise above the always present baseline due to trace impurities in the CO bottle) and due to this does not match any trend, even if there is a larger error bar for those instances where it is observed.

Table A.1: Faradaic efficiencies of observed reaction products during CORR on Ag.

Faradaic efficiencies (%):

		Ethylene glycol	MeOH	Acetic acid	EtOH	n-PrOH	H_2	CH_4	Sum
10 barg	-2 V	0.003	0.023	0.001	0.002	0.000	60.960	0.000	60.990
	-3 V	0.058	0.017	0.116	0.139	0.049	79.078	0.000	79.457
	-4.5 V	0.039	0.032	0.076	0.042	0.000	82.287	0.000	82.476
40 barg	-2 V	0.077	0.074	0.135	0.203	0.000	73.742	0.000	74.231
	-3 V	0.094	0.059	0.092	0.104	0.000	82.092	0.000	82.442
	-4.5 V	0.108	0.027	0.231	0.270	0.057	80.544	0.201	81.439
60 barg	-2 V	0.283	0.051	1.175	0.584	0.000	96.618	0.000	98.710
	-3 V	0.620	0.066	0.247	1.154	0.161	73.374	0.623	76.246
	-4.5 V	0.345	0.047	0.341	0.732	0.094	70.505	0.239	72.303

A.5. Summarized literature-reported C-C bond formation mechanisms

Reaction schemes summarizing the various proposed formation pathways for C2 and C3 products (in A3 format) are provided at the very end of the supporting information. Subsets of mechanisms proposed by the same groups have been combined into single schemes using color coding to distinguish separate publications. Different reaction mechanisms are indicated by different letters (going from A to J), combined with either -C2 or -C3 to denote if a proposed pathway leads to C2 or C3 products. Mechanisms with the same lettering are proposed by the same group(s) of people (e.g., A-C2 and A-C3 would represent the mechanism by which C2 and C3 products are formed, respectively, as proposed by the same group). References to the various publications are provided in the individual schemes, together with the color coding used for each scheme (i.e., which color belongs to which reference). Proposed reaction schemes that are similar in nature (e.g., having similar types of intermediates, overlapping steps etc.) have been grouped together as follows for C2 formation schemes: A-B, C-E, F-H, and I. The proposed mechanism J-C3 does not have a corresponding C2 mechanism, though they refer to the work represented by the mechanisms A-C2 and A-C3.

[this page has been left blank intentionally for the digital edition]

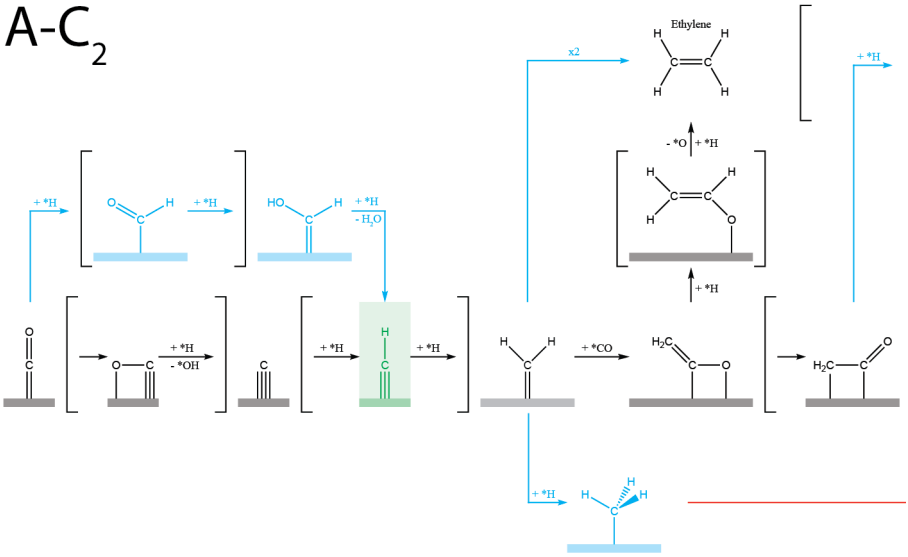

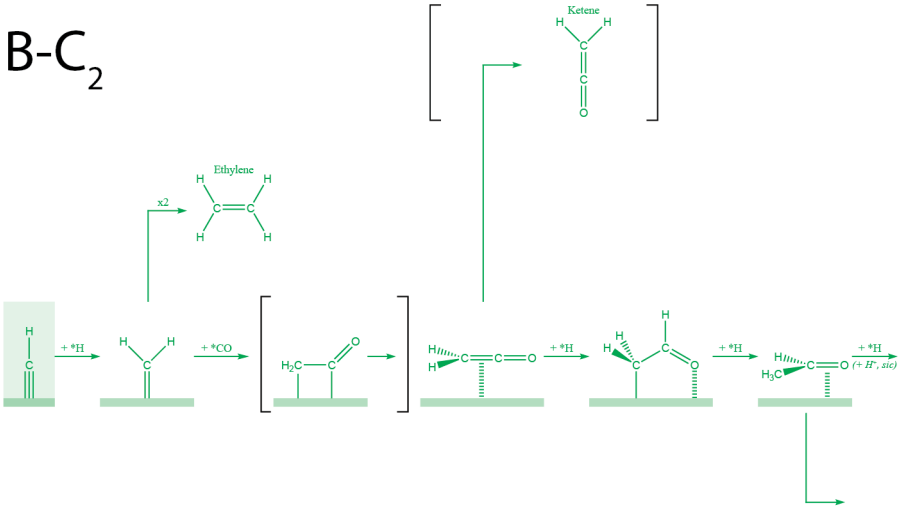

Figure A.7: Left-half

A

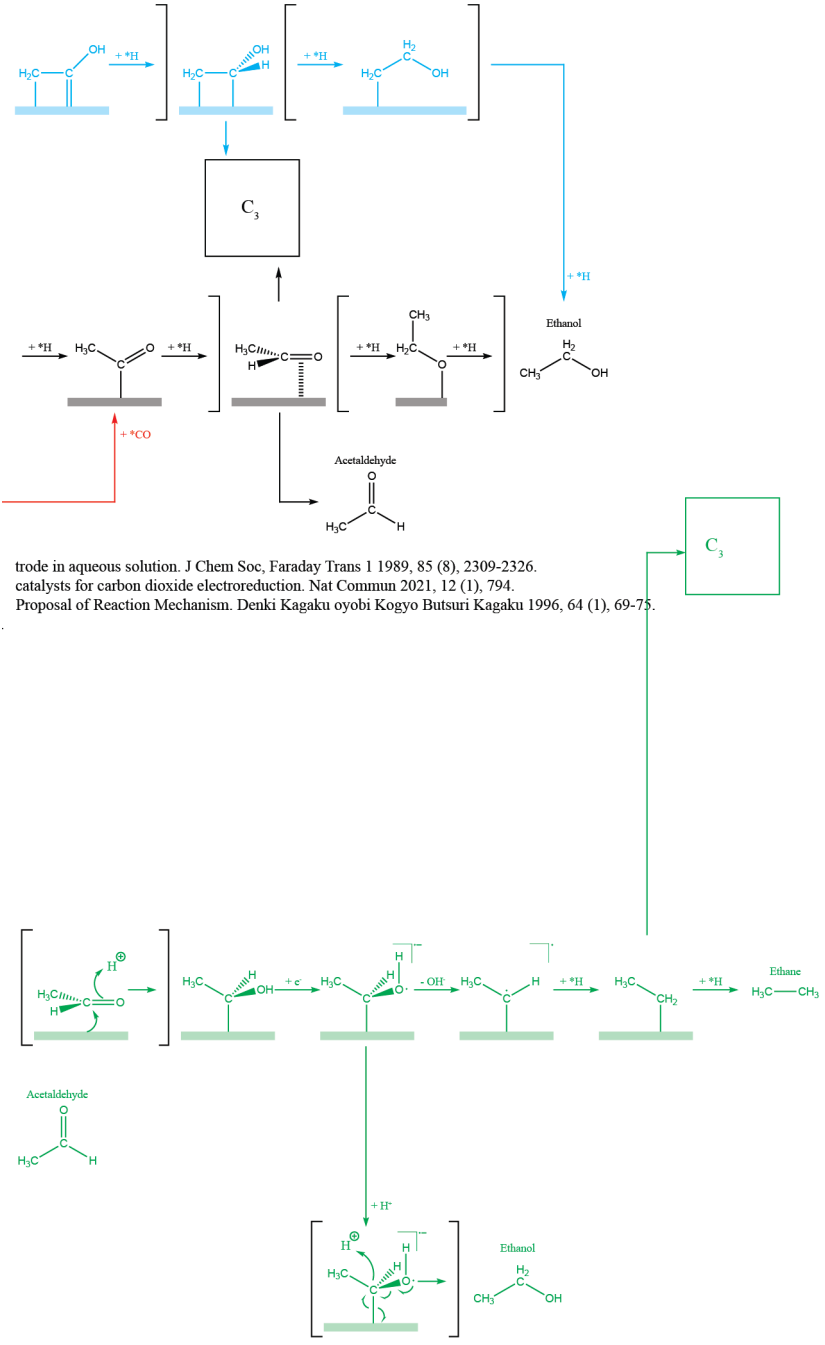

trode in aqueous solution. J Chem Soc, Faraday Trans 1 1989, 85 (8), 2309-2326.
catalysts for carbon dioxide electroreduction. Nat Commun 2021, 12 (1), 794.
Proposal of Reaction Mechanism. Denki Kagaku oyobi Kogyo Butsuri Kagaku 1996, 64 (1), 69-75.

Figure A.7: Right-half

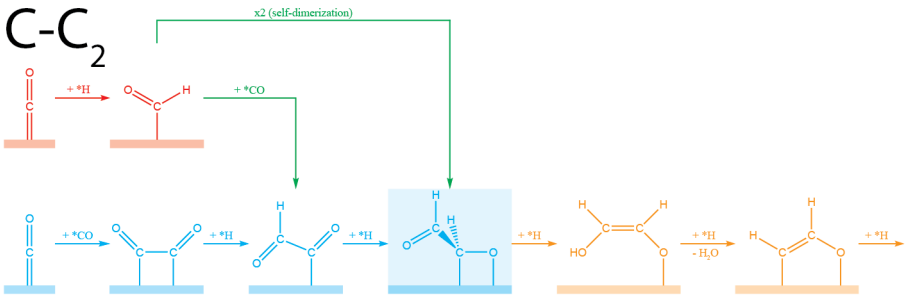

Orange Cu(211): Bertheussen, E. (Chorkendorff, I), Acetaldehyde as an Intermediate in the Electroreduction of Carbon Monoxide to Ethanol on
Red Cu(211): Peterson, A. A. (Nørskov, J. K.), How copper catalyzes the electroreduction of carbon dioxide into hydrocarbon fuels. Energy
Green Cu(211): Montoya, J. H. (Nørskov, J. K.), Insights into C-C Coupling in CO2 Electroreduction on Copper Electrodes. ChemCatChem
Blue Cu(100) & Cu(111): Montoya, J. H. (Nørskov, J. K.), Theoretical Insights into a CO Dimerization Mechanism in CO2 Electroreduction. J
Black Cu(poly): Kuhl, K. P. (Jaramillo, T. F.), New insights into the electrochemical reduction of carbon dioxide on metallic copper surfaces.

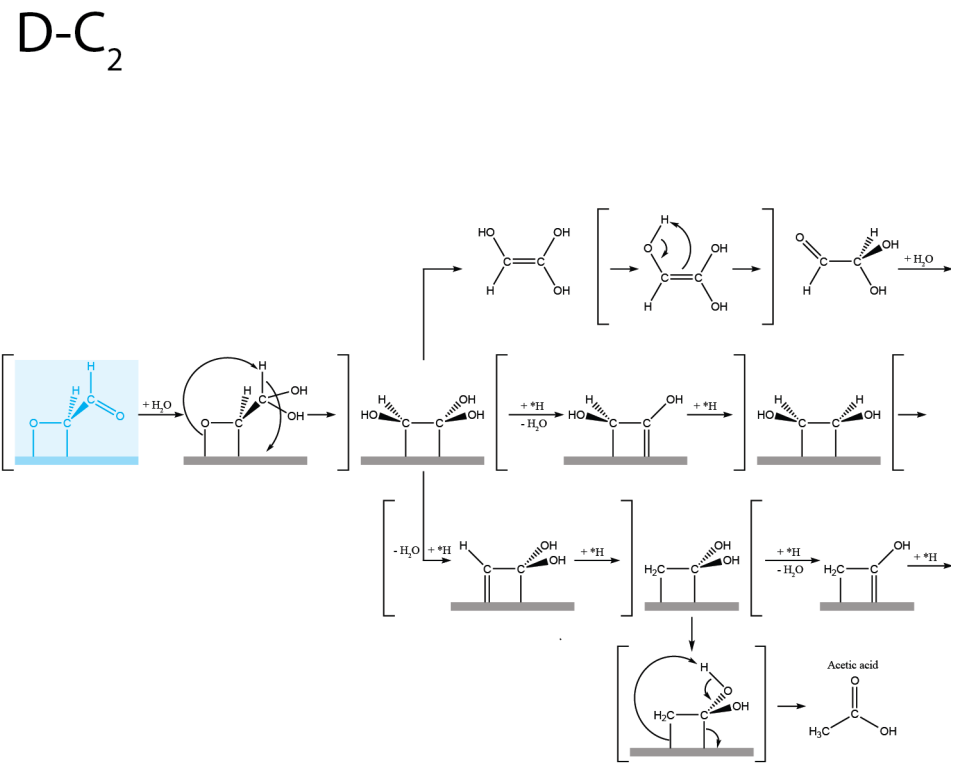

Figure A.8: Left-half

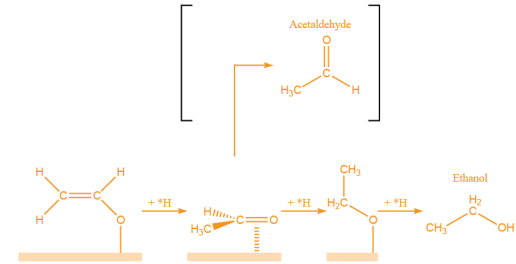

Oxide-Derived Copper. Angew Chem Int Ed 2016, 55 (4), 1450-1454.
Environ Sci 2010, 3 (9), 1311-1315.
2013, 5 (3), 737-742.
Phys Chem Lett 2015, 6 (11), 2032-2037.
Energy Environ Sci 2012, 5 (5), 7050-7059.

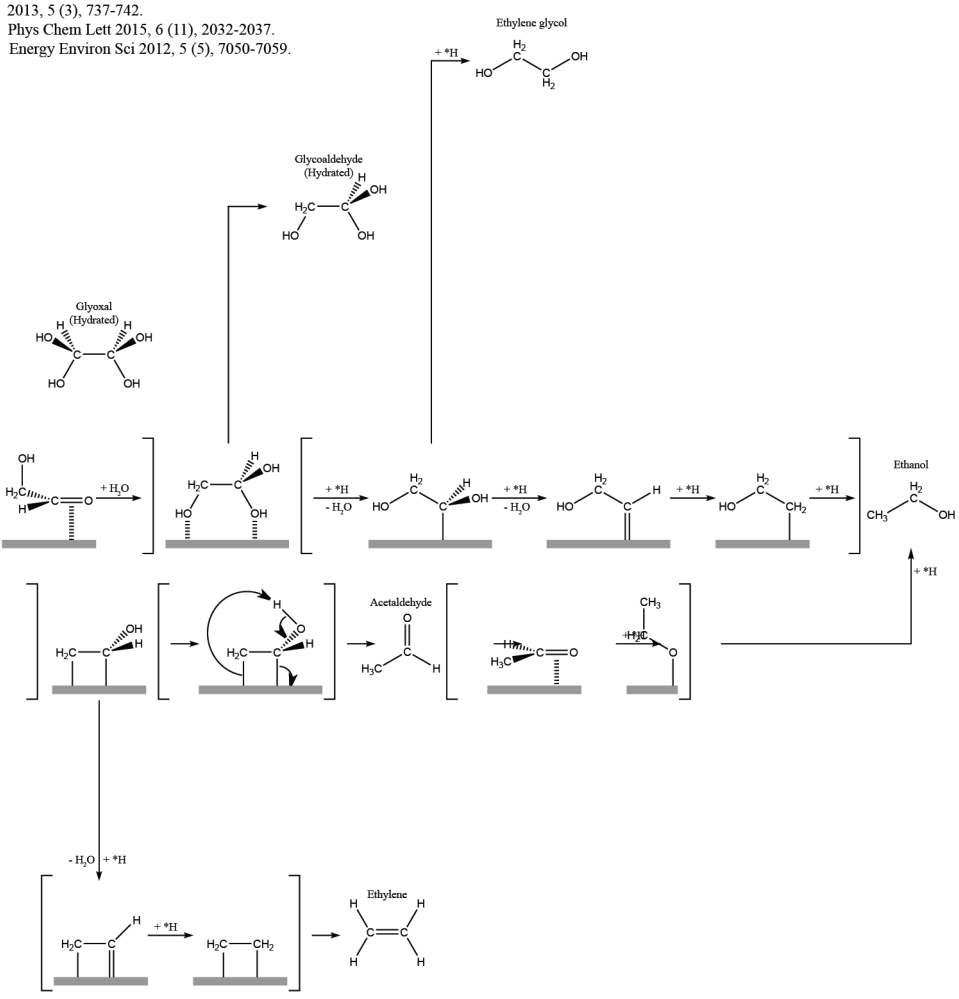

Figure A.8: Right-half

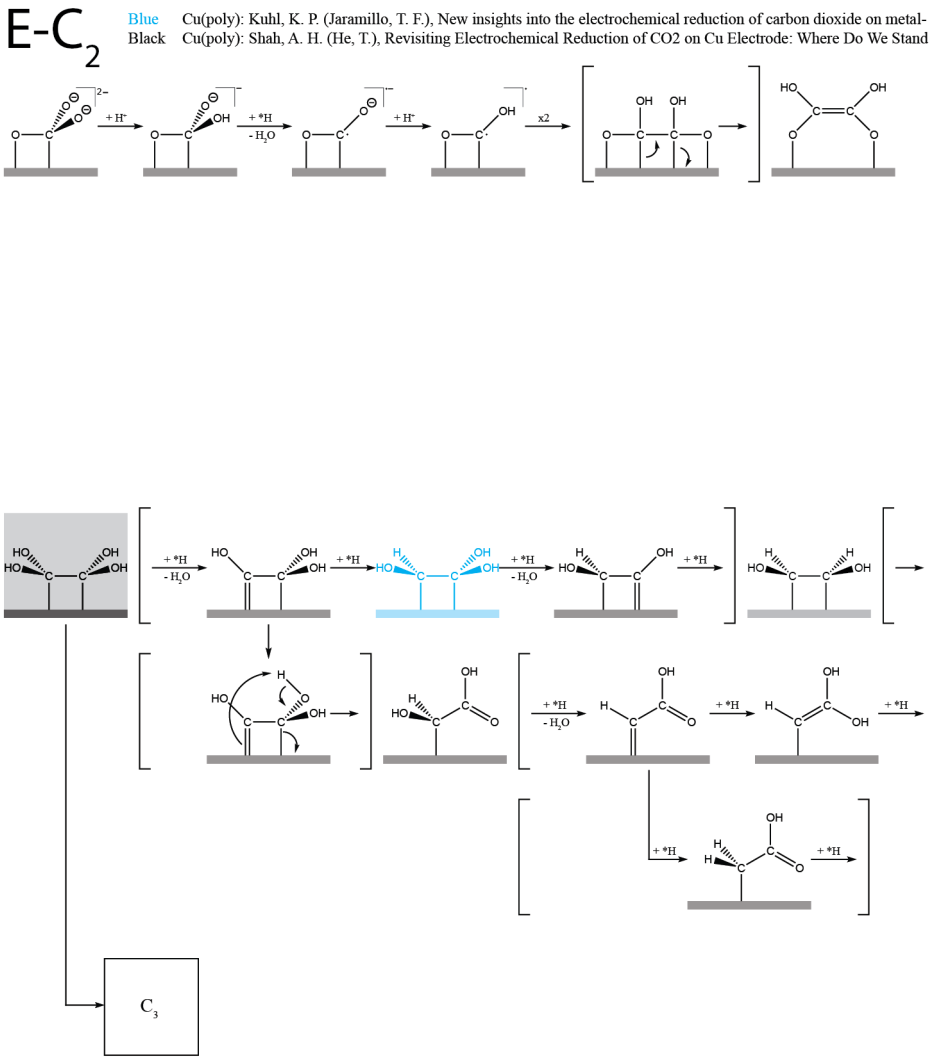

Figure A.9: Left-half

lic copper surfaces. Energy Environ Sci 2012, 5 (5), 7050-7059.
about the Intermediates? J Phys Chem C 2018, 122 (32), 18528-18536.

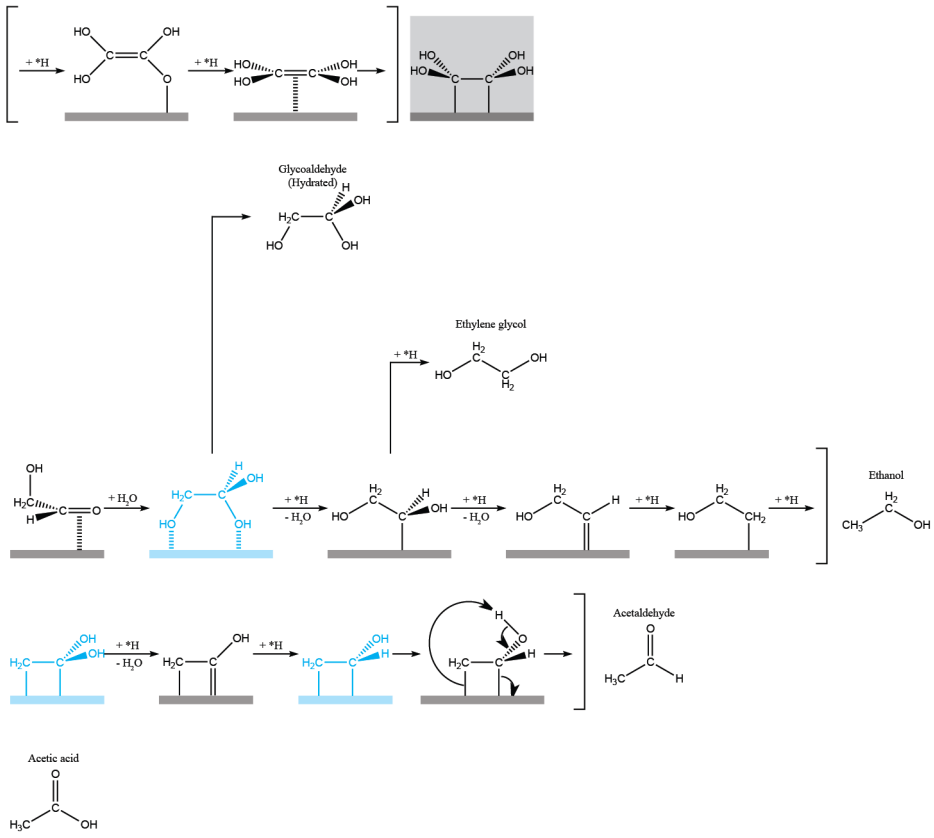

Figure A.9: Right-half

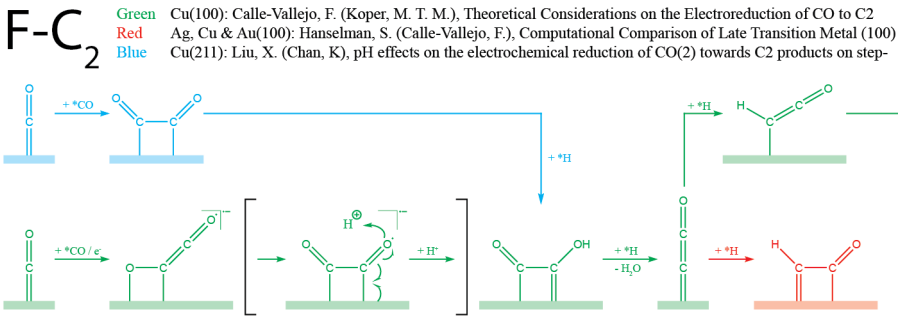

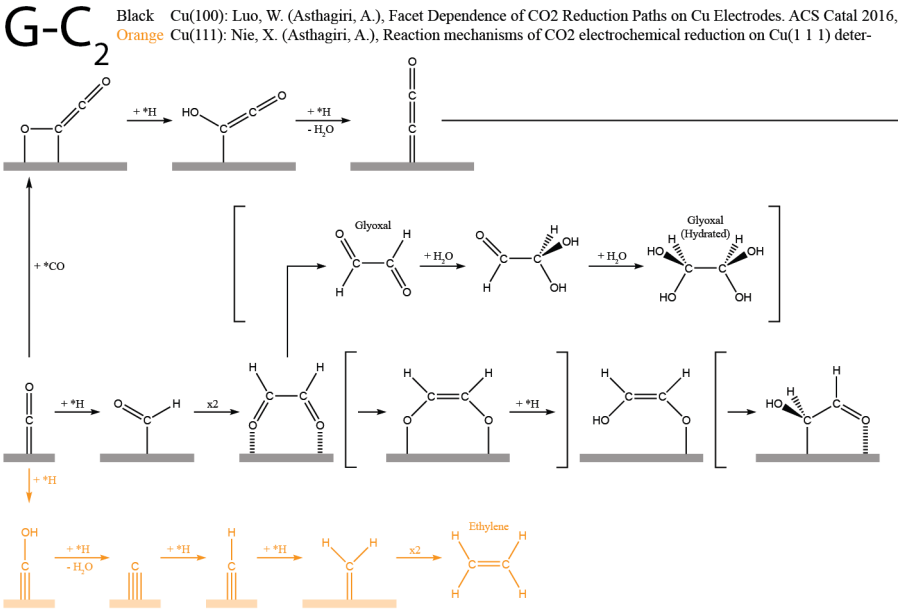

Figure A.10: Left-half

A

Species on Cu(100) Electrodes. Angew Chem Int Ed 2013, 52 (28), 7282-7285.
Surfaces for the Electrocatalytic Reduction of CO to C2 Species. ACS Energy Letters 2018, 3 (5), 1062-1067.
ped copper. Nat Commun 2019, 10 (1), 32.

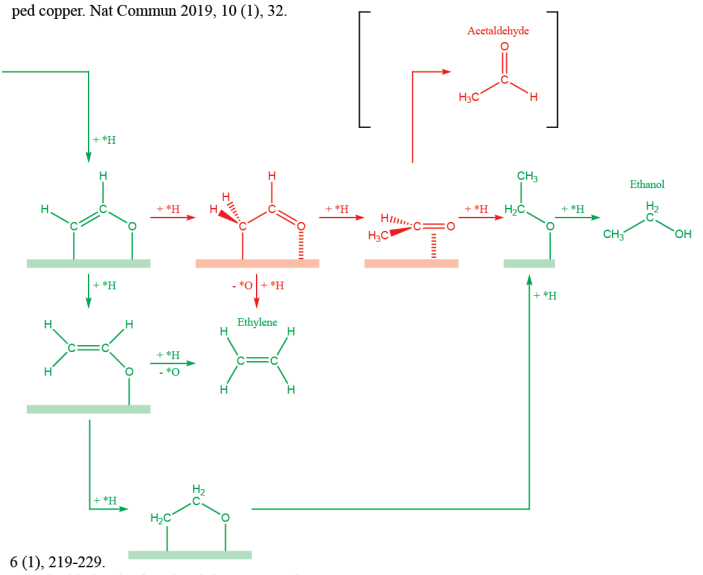

6 (1), 219-229.
mined with density functional theory. J Catal 2014, 312, 108-122.

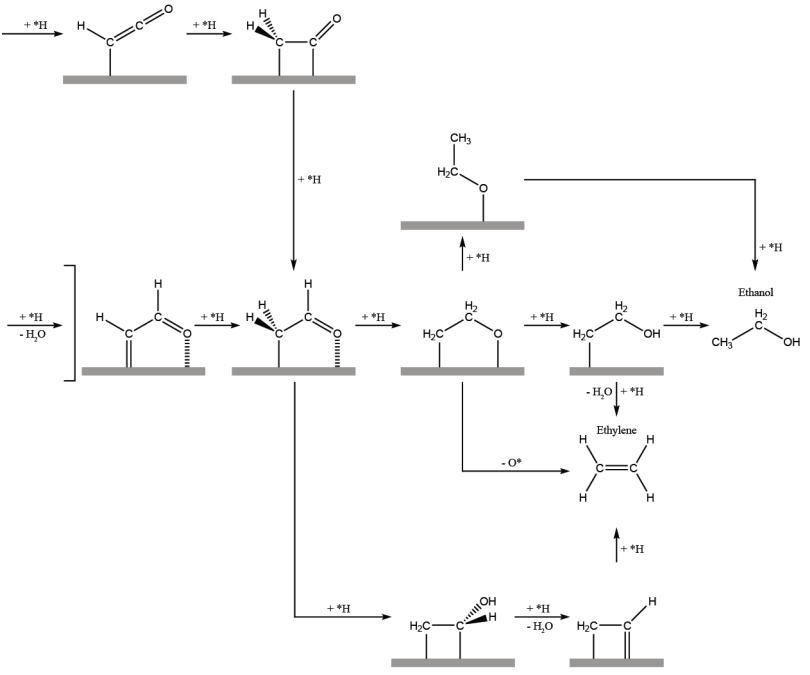

Figure A.10: Right-half

$H\text{-}C_2$ Black Cu(100): Garza, A. J.; Bell, A. T.; Head-Gordon, M., Mechanism of CO2 Reduction at Copper Surfaces: Path-
Red Only Cu(100) and only at low overpotential

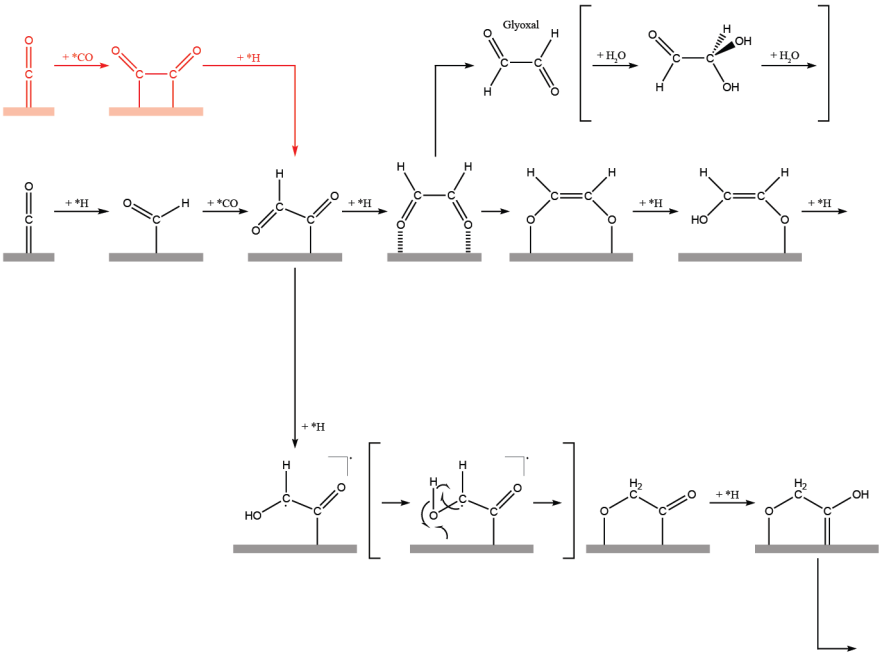

Figure A.11: Left-half

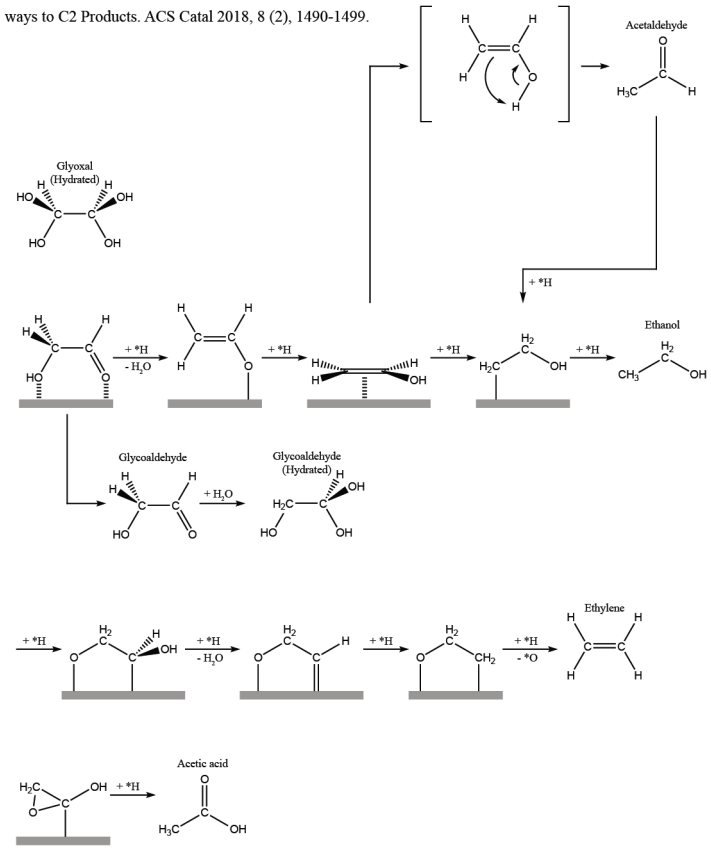

Figure A.11: Right-half

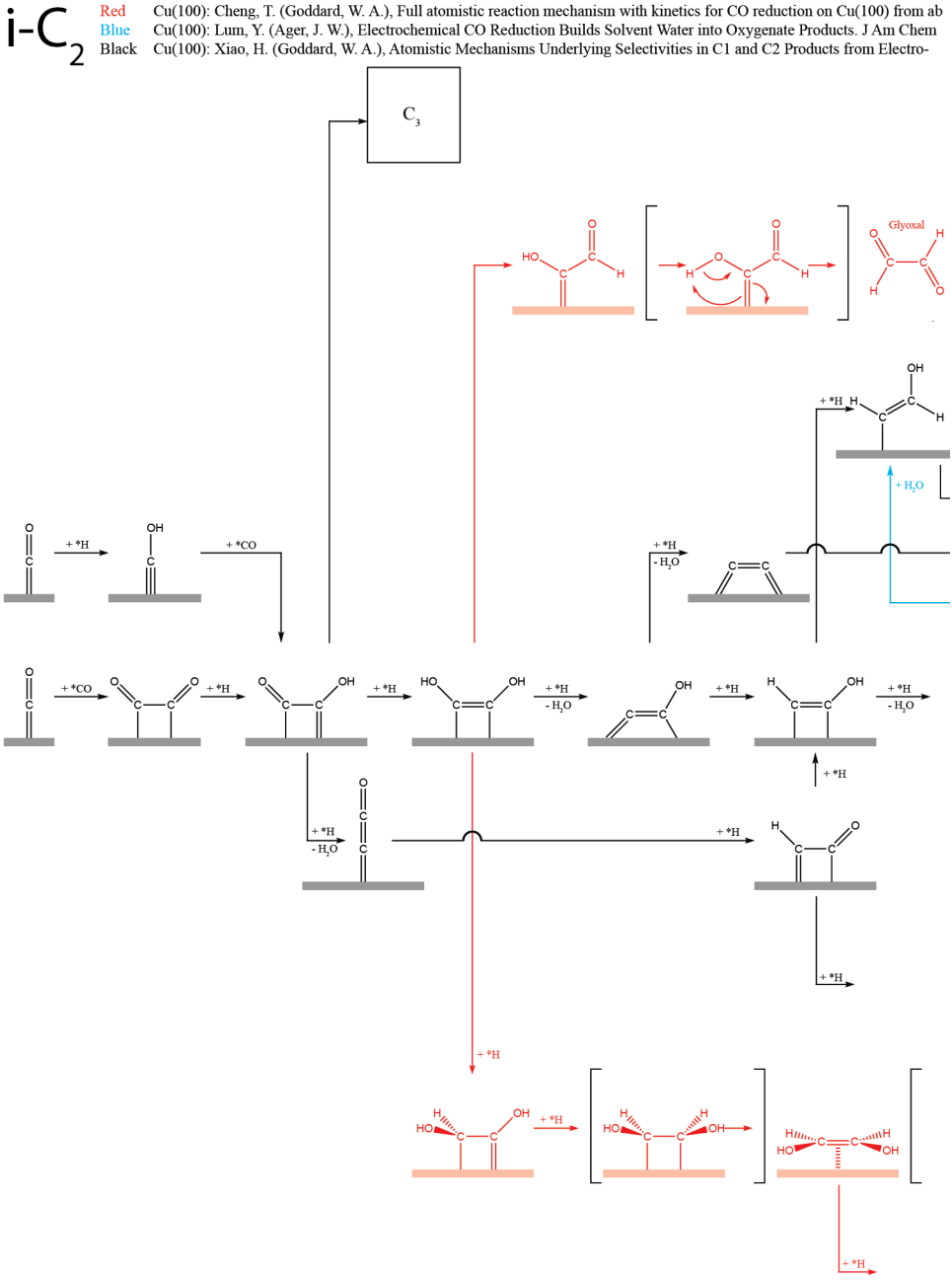

Figure A.12: Left-half

initio molecular dynamics free-energy calculations at 298 K. PNAS 2017, 114 (8), 1795-1800.
Soc 2018, 140 (30), 9337-9340.
chemical Reduction of CO on Cu(111). J Am Chem Soc 2017, 139 (1), 130-136.

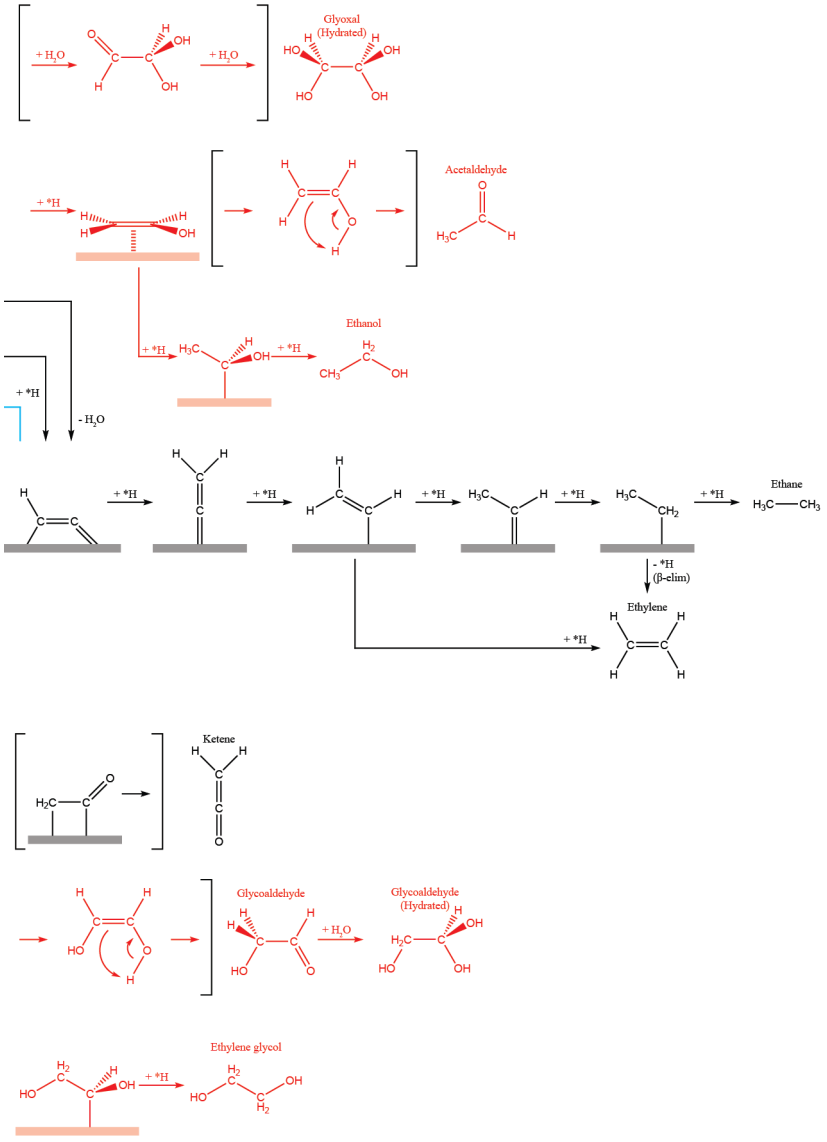

Figure A.12: Right-half

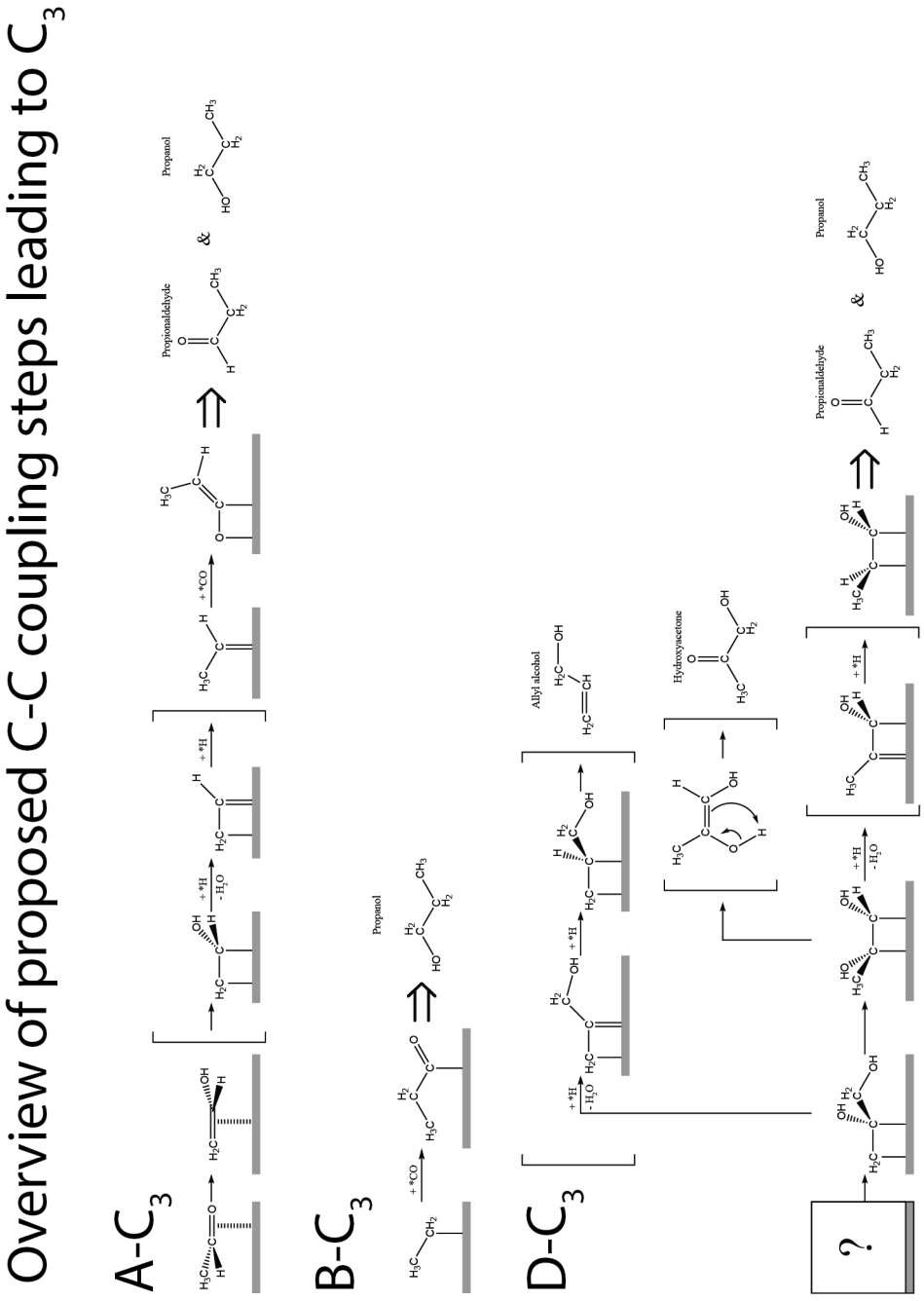

Figure A.13: Top-half

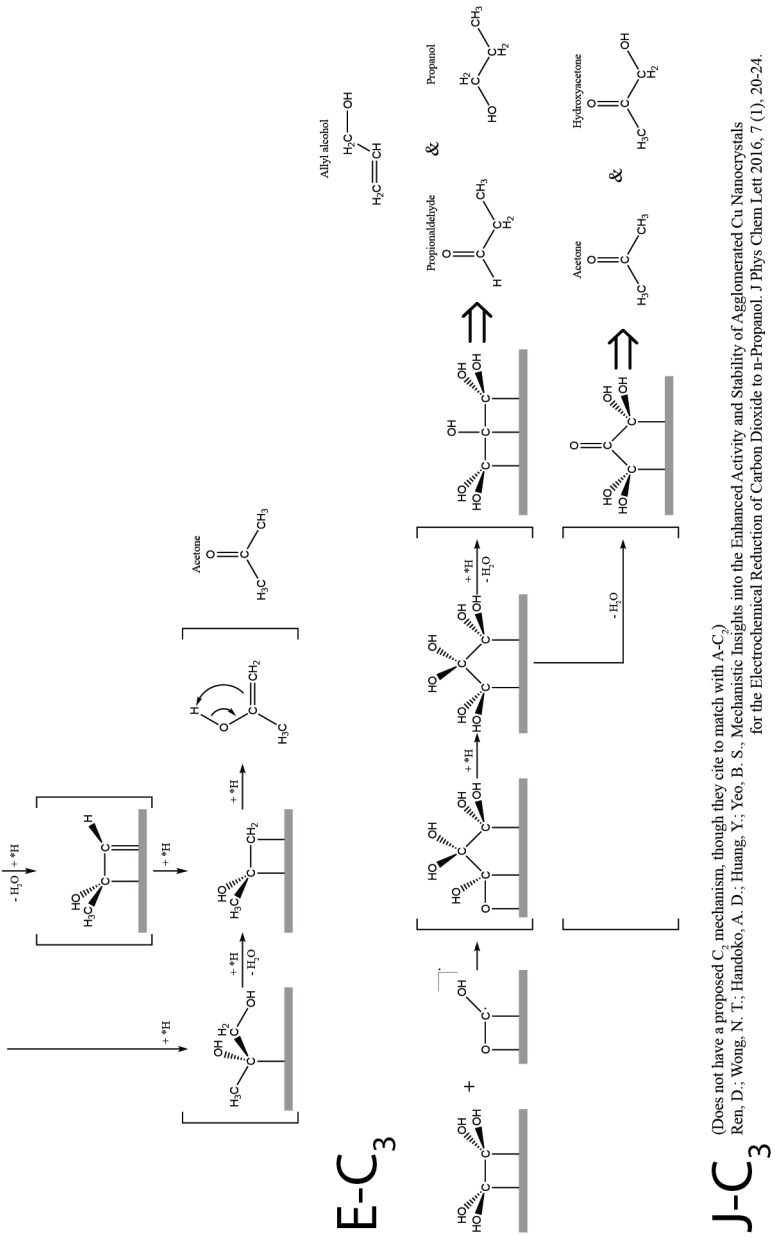

Figure A.13: Bottom-half

References

[1] Rebecca Barlag, Frazier Nyasulu, Rachel Starr, Jenna Silverman, Phyllis Arthasery, and Lauren McMills. A student-made silver–silver chloride reference electrode for the general chemistry laboratory: ~10 min preparation. *Journal of Chemical Education*, 91(5):766–768, 2014.

[2] Gaston A. East and M. A. del Valle. Easy-to-make Ag/AgCl reference electrode. *Journal of Chemical Education*, 77(1):97, 2000.

[3] Kendra P. Kuhl, Etosha R. Cave, David N. Abram, and Thomas F. Jaramillo. New insights into the electrochemical reduction of carbon dioxide on metallic copper surfaces. *Energy & Environmental Science*, 5(5):7050–7059, 2012.

[4] Esther M. Wilcox, George W. Roberts, and James J. Spivey. Direct catalytic formation of acetic acid from CO2 and methane. *Catalysis Today*, 88(1):83–90, 2003.

B

Supporting information for Chapter 3: Anisotropic Cathodic Corrosion of Gold Electrodes in Absence and Presence of Carbon Monoxide

B.1. SEM-visible onset of corrosion for {111} and {110} faces

The observable onset of corrosion for the {111} and {110} facets as visible from SEM micrographs is depicted in Figure B.1, where panels a, b represent micrographs for the {111} face prior to (no crystallites observed) and after (crystallites visible) the onset of corrosion, respectively, and panels c, d show the {110} face without pitting and with pitting (the corrosion mode for that face), respectively.

B.2. Substrate pitting of {111} and {100} faces from SEM

Although the main corrosion mode for the {111} and {100} facets is in the form of crystallite growth, the initial substrate does exhibit a certain degree of pitting as well. This is evident from Figure B.2, where panels a, b depict close-ups of the substrate beneath the crystallites for the {111} and {100} faces, respectively.

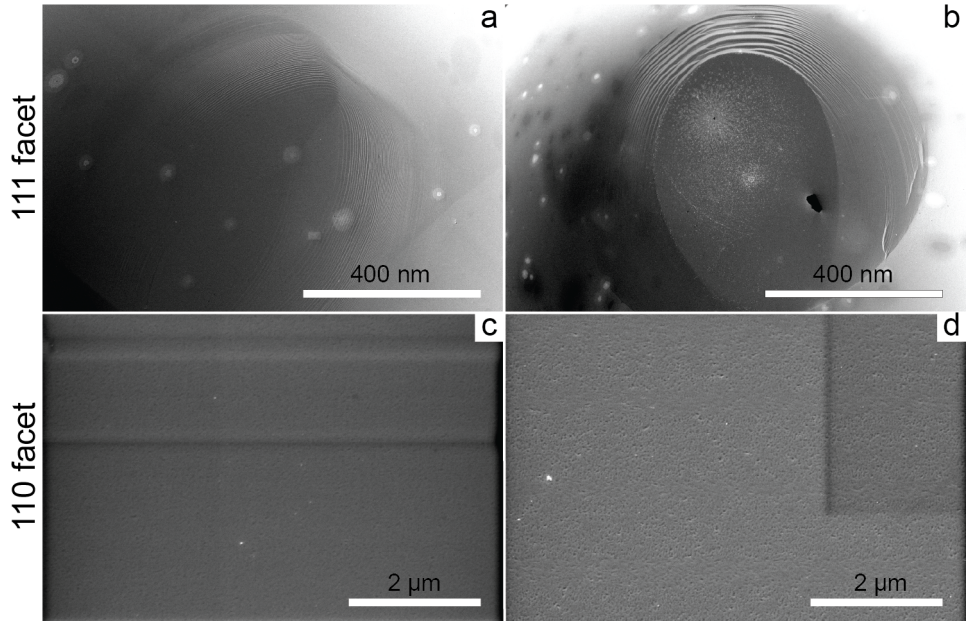

Figure B.1: Onset of corrosion-induced morphological changes as visible from SEM for the {111} facet corroded for a) 5 $minutes$ at –1.2 V_{RHE} and for b) 7.5 $minutes$ at –1.2 V_{RHE}, and for the {110} facet corroded for c) 2.5 $minutes$ at –1.1 V_{RHE} and for d) 5 $minutes$ at –1.1 V_{RHE}.

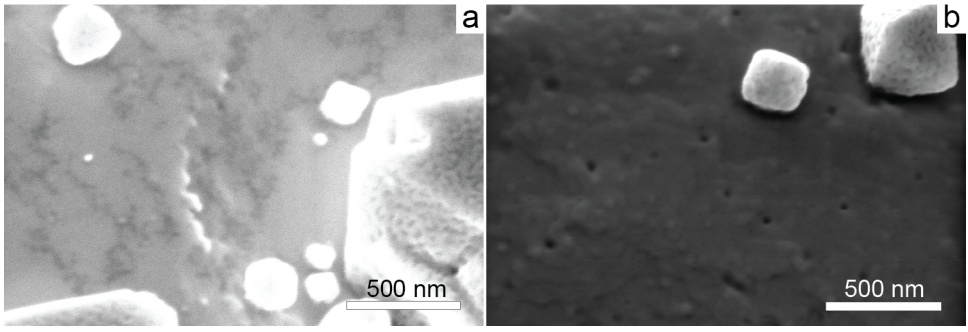

Figure B.2: Corrosion of initial substrate on which nanocrystallites grow for a) the {111} plane corroded for 7.5 $minutes$ at –1.3 V_{RHE} and b) the {100} plane corroded for 7.5 $minutes$ at –1.3 V_{RHE}.

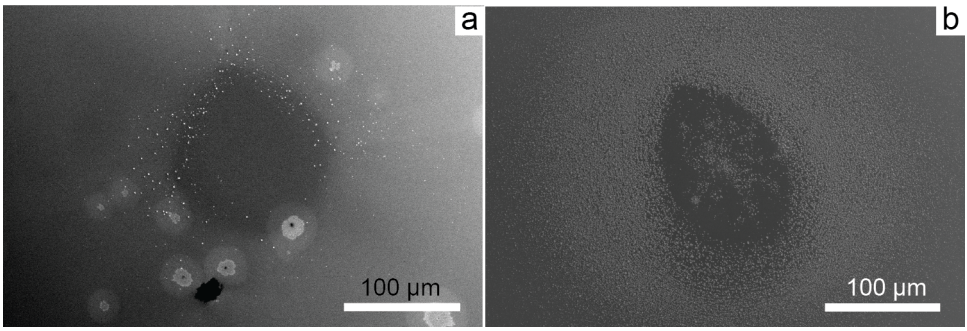

Figure B.3: Location of nanocrystallite formation on the {100} face at the early stages of corrosion after a) 2.5 $minutes$ at –1.3 V_{RHE} and for longer corrosion times; i.e., for b) 5 $minutes$ at –1.3 V_{RHE}.

B.3. Onset location crystallites {100} face

Although corrosion of the {100} face results in crystallite formation on and near this face, growth starts from the edges of this face at the onset of corrosion as depicted in Figure B.3 where in panel a is shown a micrograph obtained near the observed onset of crystallite formation and is compared to corrosion for extended time in panel b. It can be seen that initially crystallites form at the edges of the facet, whereas for longer corrosion times crystallites form also on the actual {100} face.

B.4. Absence of crystallite formation during extended corrosion at decreased cathodic potential

Proof that crystallite formation is not the result of dissolution and redeposition of the counter electrode is provided in the form of long-term corrosion at (slightly) decreased cathodic potentials in Figure B.4. This is evident from the global overview of a spherical single crystal when –1 V_{RHE} is applied for 1.5 $hours$ in the presence of CO. Although considerable contamination is present (in the form of white 'blobs'), no crystallites were observed on this surface.

B.5. Imperfect double layer signals for cut Au crystals

The double layer signals for the (cut) single crystalline surfaces we employ in this work (Figure B.5) differ from established literature for the single crystalline gold basal planes (although the important features are present).[1–6] We attribute the deviations with respect to specifically the double layer region to mainly two points. Firstly; the crystals used herein started off with a certain fraction of defect sites which affects average terrace sizes and adds new types of adsorption sites and, secondly; minute traces of oxygen were present in the electrolyte during some of

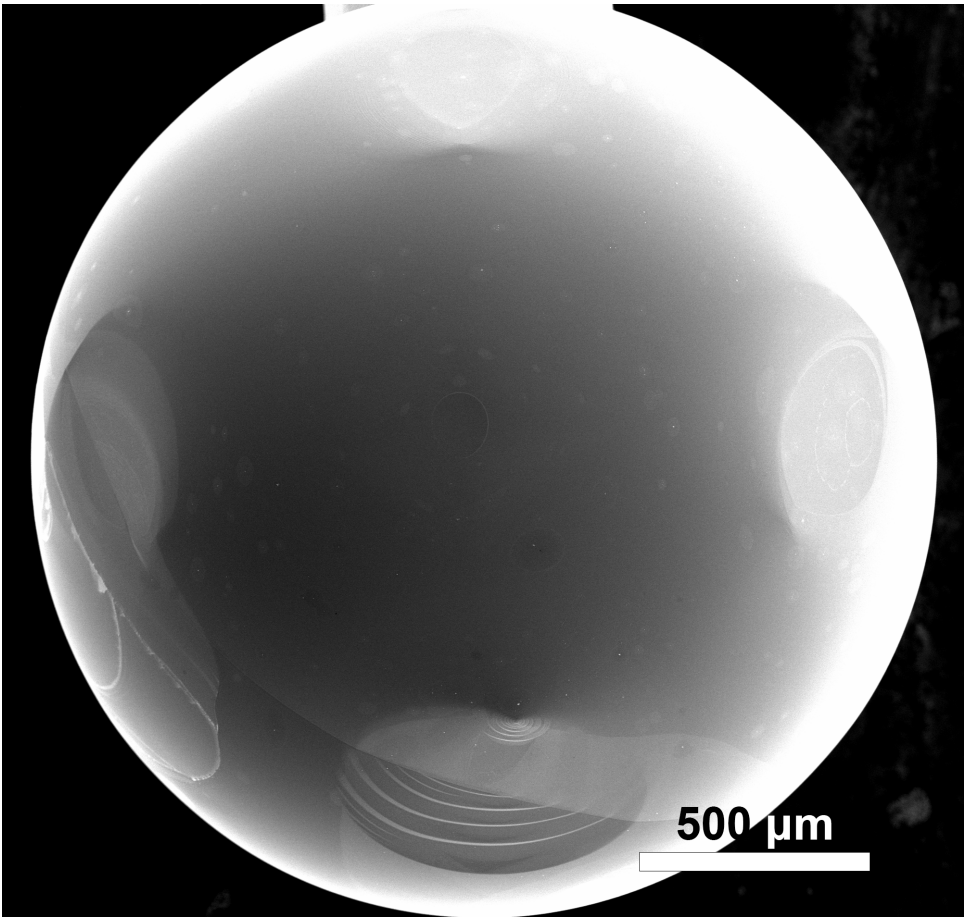

Figure B.4: Overview of a gold spherical single crystal after corrosion for 1.5 $hours$ at –1 V_{RHE} in the presence of CO.

the measurements. Additionally, the scan rate employed in this work ($80\ mV{\cdot}s^{-1}$) is also different from what is commonly used in double layer investigations ($10\ mV{\cdot}s^{-1}$) which influences charging currents. Finally, an imperfect meniscus, which would expose a small fraction of the sides of the crystal, may also result in the behavior of the double layer observed. The presence of defect sites is seen also in the gold oxide region, evident from current in the potential regions attributed to step-sites as described in Table 3.1 (main text). To the best of our knowledge, there exists no literature that systematically investigates the changes of the double-layer region when step-site defects are introduced. Irrespectively, as can clearly be seen from the hydroxide/oxide adsorption regions as shown in this work, the majority feature for the differently cut single crystals matches the feature that is attributed to the respective basal planes.

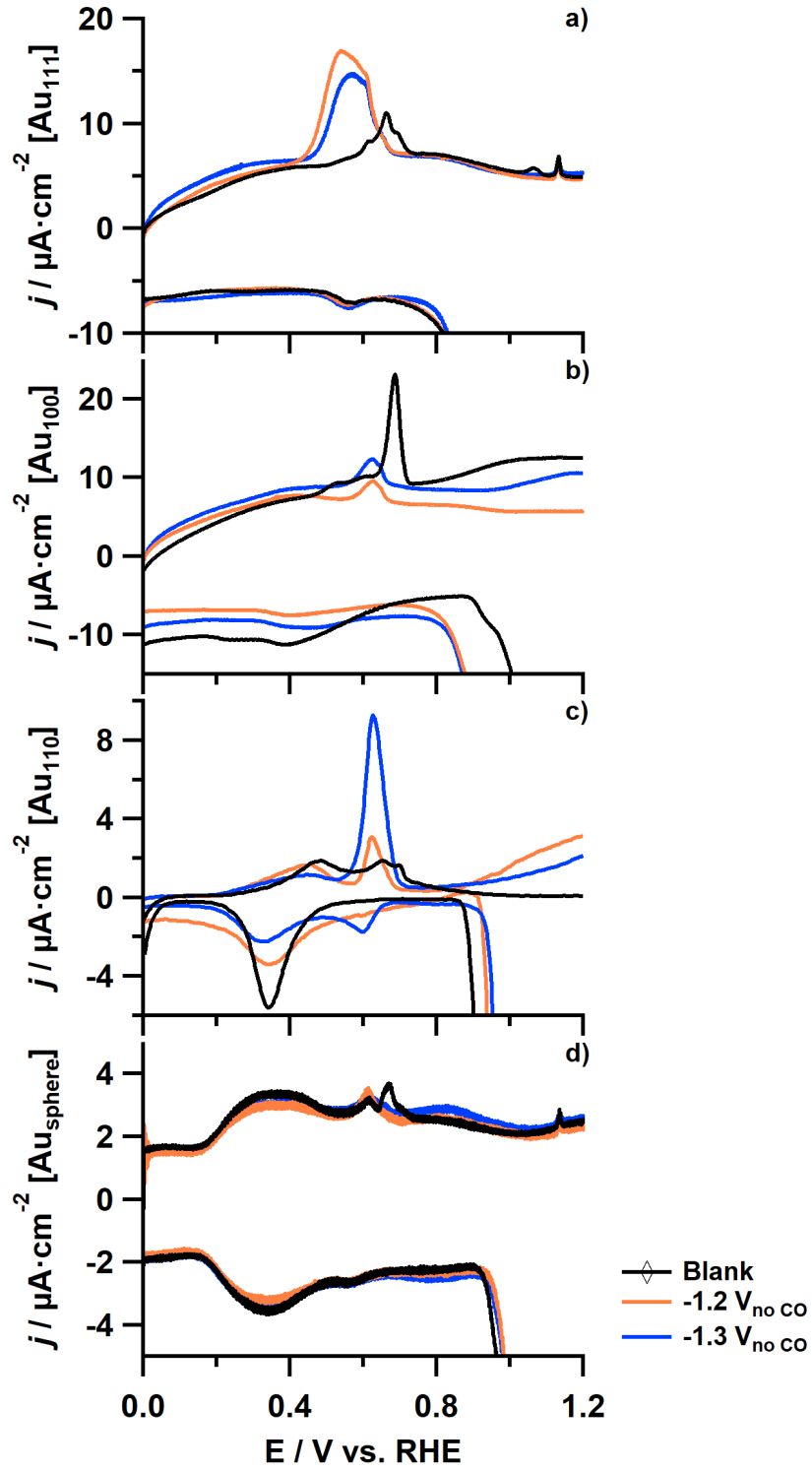

Figure B.5: Zoom of the CV DL region for gold crystals corroded in 10 M NaOH for 2.5 $minutes$ in the absence (solid lines) and presence (dashed lines) of CO at –1.2 V_{RHE} (orange) and –1.3 V_{RHE} (blue) (85% iR corrected) for a) Au(111), b) Au(100), c) Au(110) and d) Au(spherical) electrodes, compared with their respective CVs prior to corrosion (black).

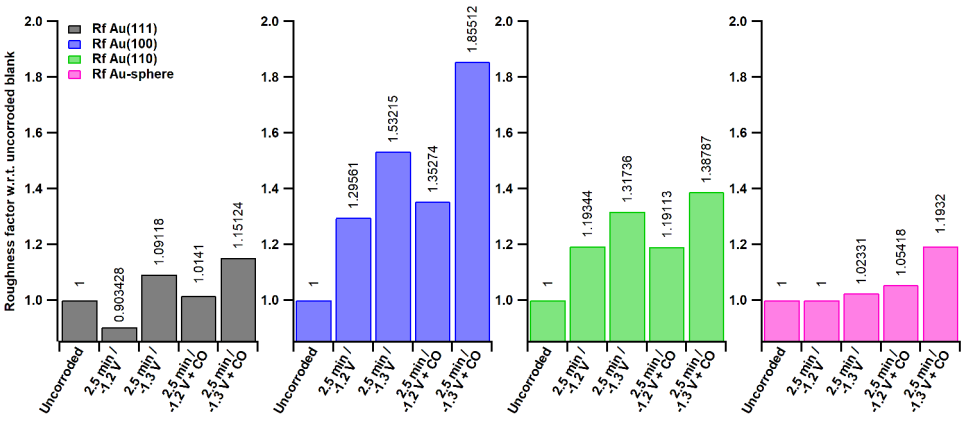

Figure B.6: Roughness factors for crystals with different crystallographic orientations (Au(111), black bars; Au(100), blue bars; Au(110), green bars; Au(sphere), pink bars) before and after cathodic corrosion in $10\ M$ NaOH for $2.5\ minutes$ at –1.2 and –1.3 V_{RHE}, in the absence and presence of CO (going from left to right).

B.6. Crystal roughness determination

Roughness factors after corrosion (see Figure B.6) were determined by integrating the oxidation current in the CV obtained after corrosion at potentials more positive than $0.9\ V$ vs. RHE after subtraction of the double layer current, and dividing this charge by the charge that was similarly calculated from the CV obtained prior to corrosion. The double layer current was determined either mathematically via eq. B.1 for CVs that exhibited a symmetrical double layer region between $0 < E < 0.15\ V$ vs. RHE, or otherwise by manually shifting the CV down whilst carefully considering that the oxidation current in the region between $0.9 < E < 1.3\ V$ vs. RHE didn't fall below zero.

$$i_{DL} = \frac{1}{2} \cdot (\bar{i}_{\text{forward}} - \bar{i}_{\text{backward}}) \text{ between } 0 \leq E \leq 0.15\ V \tag{B.1}$$

References

[1] T. H. Dretschkow and T. H. Wandlowski. The kinetics of structural changes in anionic adlayers on stepped Au(111)s electrodes from sulfuric acid solutions. *Berichte der Bunsengesellschaft für physikalische Chemie*, 101(4):749–757, 1997.

[2] Ludwig A. Kibler. *Preparation and characterization of noble metal single crystal electrode surfaces*. International Society of Electrochemistry, 2003.

[3] D. M. Kolb. Reconstruction phenomena at metal-electrolyte interfaces. *Progress in Surface Science*, 51(2):109–173, 1996.

[4] O. M. Magnussen, J. Wiechers, and R. J. Behm. In situ scanning tunneling microscopy observations of the potential-dependent (1 × 2) reconstruction on Au(110) in acidic electrolytes. *Surface Science*, 289(1):139–151, 1993.

[5] H. Striegler, P. Skoluda, and D. M. Kolb. On the stability of unreconstructed Au(100)-(1×1) at negative potentials in aqueous sulfate solution. *Journal of Electroanalytical Chemistry*, 471(1):9–13, 1999.

[6] Koji Yoshida, Akiyoshi Kuzume, Peter Broekmann, Ilya V. Pobelov, and Thomas Wandlowski. Reconstruction and electrochemical oxidation of Au(110) surface in 0.1 M H2SO4. *Electrochimica Acta*, 139:281–288, 2014.

C

Supporting information for Chapter 4: Clean and Reproducible Voltammetry of Copper Single Crystals with Prominent Facet-Specific Features Using Induction Annealing

C.1. Copper cleaning and characterization

Two different cleaning methodologies were employed in this work. The first cleaning method is a commonly employed electropolishing[1–3] treatment, and was conducted on disk-type Cu(poly) electrodes. Briefly, the copper disk was polished with increasingly smaller sizes of alumina polishing paste (Buehler) on polishing cloth (Buehler), starting at $5\ \mu m$ and decreasing down to $1\ \mu m$ on a polishing machine until a shiny finish was obtained. Thereafter, the electrode was rinsed with and subsequently sonicated in Milli-Q water for at least $15\ min$. Finally, the surface was electropolished at $+3\ V$ vs. a graphite CE (99.9995%, metals basis, Alfa Aesar) in $66\ wt\%$ H_3PO_4 prior to electrochemical characterization (described in a later section).

The second cleaning method (used for all other surfaces in this work) is as follows. Copper electrodes were rinsed with Milli-Q water and then placed in an isolated induction annealing compartment with gas inlets and a water-locked gas

outlet for controlled-atmosphere annealing. Reductive atmosphere was applied by purging pure H_2 (Linde 5.0) for disk-type single crystals, or a mix of H_2 and Ar of ca. $50:50\ vol\%$ for spherical bead-type Cu(poly) crystals, with the total gas flow kept at $300\ sccm$ (standard cubic centimeters per minute) via mass flow controllers. Mixing hydrogen and argon was necessary for spherical bead-type Cu(poly) crystals due to instrument power limitations with the required gas ratio depending on crystal dimensions, but the argon content was kept as low as possible due to the trace oxygen impurities commonly present in argon. The power of the RF-heating instrument was adjusted to fine-tune crystal temperature as judged by the color, with crystals being heated to having an orange-to-yellow glow ($950 \pm 50\ ^\circ C$) and kept there for ca. $5\ min$. After annealing, electrodes were quench-cooled in pure hydrogen for ca. $5\ minutes$ (methodology: increase H_2 flow to $1000\ sccm$, halt Ar flow, stop induction current), although cooling time was increased for crystals annealed for longer periods because of increased heating of the surrounding parts. The exact setup is depicted in Figure C.1, which is based on the designs of others as previously reported[4–8], with the key difference being the introduction of a valve that allows for uncoupling the annealing environment from the electrochemical cell.

After the crystal had reached room temperature, an internal pathway from the annealing section (compartment 1, Figure C.1) to the electrochemical cell below (compartment 2, Figure C.1) was established by turning a key with a sufficiently large keyhole to allow for the crystal to pass through. At this point the argon flow through the electrolyte ($0.1\ M$ NaOH) is halted, and instead argon flow is directed to blanket the electrolyte. By opening the key, the annealing compartment and electrochemical cell are now internally connected and thus their initially separate atmospheres can mix; $1000\ sccm$ of H_2 of the annealing compartment (on top) with Ar from the bottom compartment (argon flow was manually adjusted until the electrolyte surface was close to vibrating due to the gas pressure, exact flowrate unknown). Prior to lowering the crystal and closing the electrical circuit, an 'insertion potential' was pre-applied. The electrode was lowered through the keyhole, and a meniscus established under electrochemical control. After establishing electrochemical contact, the hydrogen flow in the annealing section is halted and replaced by $1000\ sccm$ of argon. The electrochemical steps and applied potentials vary slightly with the crystallographic orientations of the crystals, and are described in detail in the following subsections.

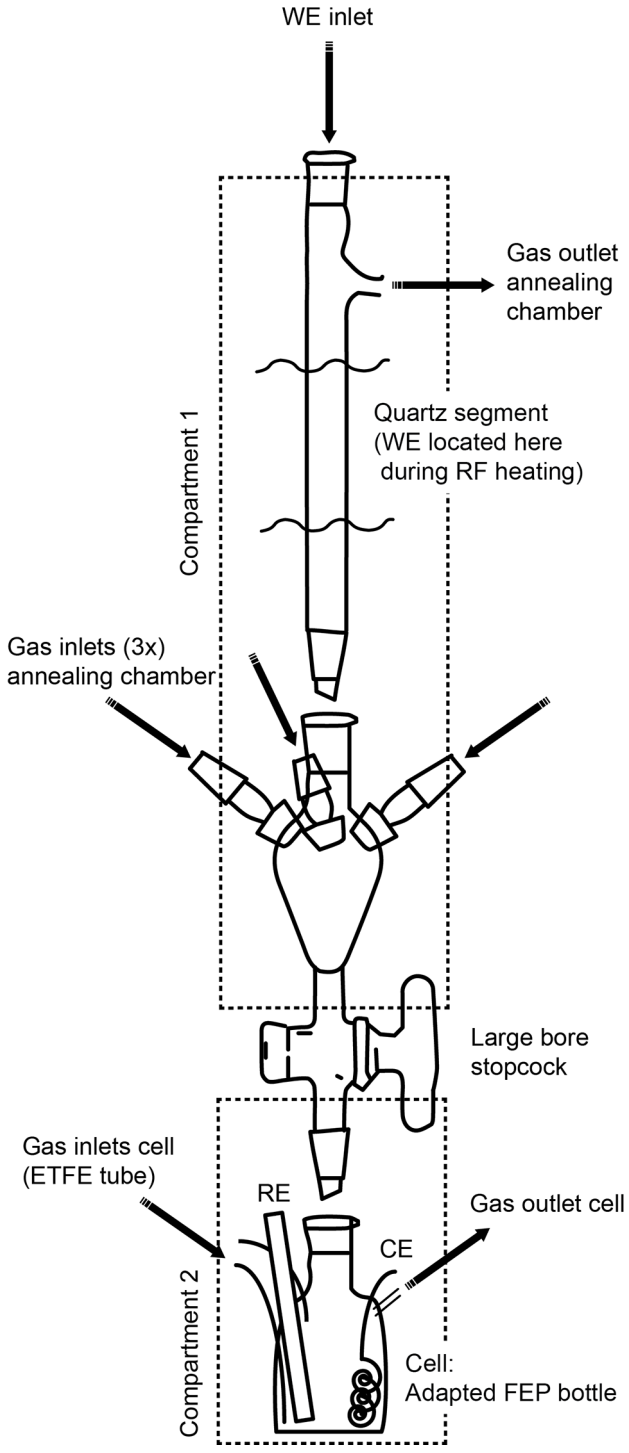

Figure C.1: Components that make up the controlled atmosphere induction annealing + electrochemistry setup. All parts not specifically labeled are made out of borosilicate glass.

C.1.1. Cu(100) characterization

By following the methodology described in this section, stable and symmetrical CVs for Cu(100) electrodes should be obtained, given clean and oxygen-free atmosphere and electrolyte.

a. Establish initial electrochemical contact with the electrolyte at $0\ V$ vs. RHE (i.e., apply $0\ V$ prior to closing the electrical circuit). After establishing contact, adopt a hanging meniscus configuration and allow for the contact current to decrease and stabilize; ca. $-100\ pA \cdot cm_{geo}^{-2}$ is normally achieved in properly deaerated electrolyte solution after 1 to $15\ minutes$.

b. After reaching a sufficiently low and stable contact current, conduct a linear sweep (LS) from $0\ V$ to $-0.25\ V$ (scan rate $\nu = 50\ mV \cdot s^{-1}$).

c. At this point, start a pre-cycling period in order to stabilize (and possibly reconstruct, when accidentally starting with a slightly oxidized crystal) the {100} terraces. Scan in the potential window $-0.25\ V < E < +0.35\ V$ vs. RHE at a scan rate $\nu = 50\ mV \cdot s^{-1}$ for a number of times (ca. 5) to obtain a symmetrical {100}-feature at $-0.125\ V$. For a properly annealed and (mostly) defect-free crystal, pre-cycling CVs should change little, if at al.

d. After pre-cycling, measure one final CV in the potential window $-0.25\ V < E < +0.50\ V$ at scan rate $\nu = 50\ mV \cdot s^{-1}$ (the characterization CV).

This final window was chosen to encompass the known adsorption features of {111}, {100} and {110} sites, but leads to irreversible changes for certain facets. Hence, after measuring this full window it is important to rinse and reanneal the surface. The surface after reannealing will be identical to the surface as characterized via CV in the final step. Alternatively, one can either halt at step c) and work with that surface without the need for reannealing, or decrease the upper potential limit in step d) to $+0.44\ V$ and continue without the need for reannealing.

C.1.2. Cu(111) and Cu(poly) characterization

A defining characteristic of (surfaces containing) {111} terrace sites is the fact that those particular sites seemingly reconstruct when fixed potentials are applied for extended periods of time ($> 10\ s$). In practical terms, if the (any) potential is held constant for protracted periods, the {111}-specific OH-adsorption feature is found to diminish in intensity, and traces of an additional (cathodic) feature start to manifest. This effect is more pronounced if the potential is scanned to $E < -0.15\ V$, and very clear when comparing the CV of a polycrystalline electrode that was actively cycled without a standby period with an electrode that was firstly kept at $-0.25\ V$ for ca. $60\ seconds$ before commencing cycling (Figure C.2, black and red lines, respectively). Specifically, it can be seen that the main {111} terrace feature at $+0.1\ V$ for the black line exhibits increased current density, and the red line shows a cathodic 'shoulder' near ca. $+0.025\ V$. Although these measurements were conducted on two different crystals (with the red line specifically having some inaccuracy in its calculated electrochemically active surface area due to traces of

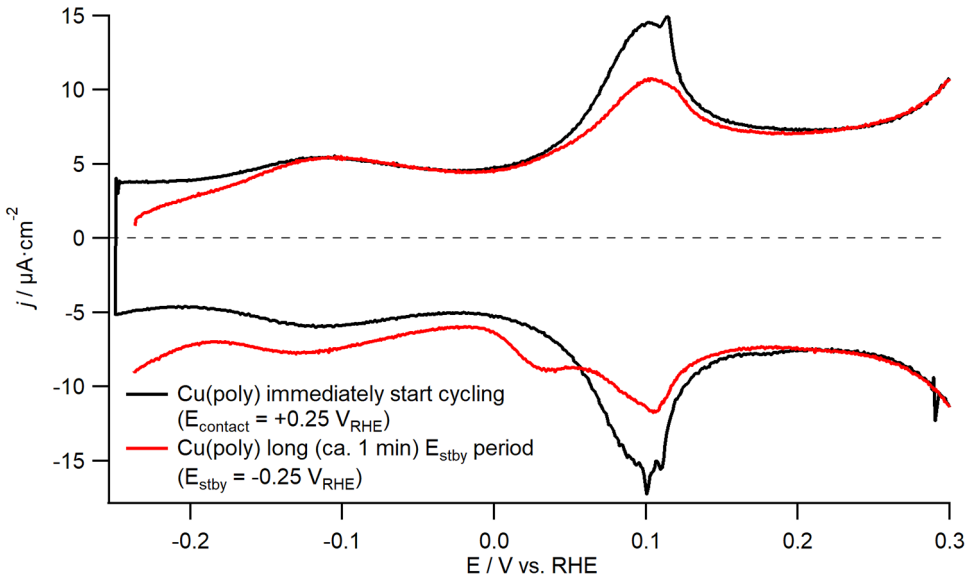

Figure C.2: Comparison of two Cu(poly) electrodes, one measured with only a brief ($< 10\ s$) standby period ($+0.25\ V$) followed by active cycling ($-0.15\ V < E < +0.425\ V$, black) and one measured after a prolonged standby period ($-0.25\ V$, ca. $90\ s$) followed by active cycling ($-0.25\ V < E < +0.425\ V$, red).

oxygen), the differences between them are representative of what is observed if the same surface would be subjected to the two different initial treatments.

Currently, we are unsure as to what causes this behavior, and what these differences mean exactly for the state of the surface. However, staying at a fixed potential for prolonged periods of time results in a weakening in intensity, decreased reversibility and the development of an additional cathodic feature. These signs are all opposite of what one would expect for a single crystalline surface of high quality; considering those generally exhibit high reversibility and intense facet-specific features. Therefore we consider the surface obtained without a standby period to be better representative of clean {111} terrace sites with long-range ordering, especially considering that those CVs compare favorably with recent literature reported voltammograms on a UHV-prepared Cu(111) crystal.

One can obtain voltammograms with a pronounced {111}-terrace specific adsorption feature by initiating the measurement with only a brief standby period followed by cycling – a methodology that is employed by Sebastián-Pascual *et al.*[9, 10] (provided in greater detail to us in a personal communication), which served as the basis for the procedure used in this work as described below.

a. Make initial electrochemical contact with the electrolyte at $+0.25\ V$ vs. RHE for Cu(111)/Cu(poly) electrodes. However, immediately after establishing electrolyte contact and making the meniscus (a process that should take only a few seconds), sweep the potential from $+0.25\ V$ to $-0.15\ V$.

b. After reaching $-0.15\ V$, start a pre-cycling period in the potential window $-0.15\ V < E < +0.425\ V$. This pre-cycling step is necessary to allow for the sides of the crystal to dry and any ORR-related current to diminish, as no stabilization period at any fixed potential was found usable. Generally, a total of 5 cycles was sufficient for the CV to become symmetrical around the x-axis, denoting the absence of oxygen-related current. Similarly to Cu(100), the pre-cycling CVs should change little, if at all, for a properly annealed and (mostly) defect-free crystal. However, the main {111} terrace feature around $+0.1\ V$ is very sensitive to the presence of electrolyte contamination and/or surface defects, which manifests itself in a decrease in charge of the OH-adsorption feature with successive cycling. Generally, increasing argon flow, reannealing the crystal or replacing the electrolyte was found to remedy this.

At this point, the methodology diverges for Cu(111) and polycrystalline surfaces. Cu(111):

c. After the pre-cycling period, measure one final CV in the potential window $-0.15\ V < E < +0.50\ V$ at scan rate $\nu = 50\ mV \cdot s^{-1}$ (the characterization CV). Please note that the cathodic boundary is slightly more positive than for Cu(100), since the {111} terraces were found to be unstable at potentials $E < -0.15\ V$.

Cu(poly):

c. After pre-cycling, extend the lower CV boundary from $-0.15\ V$ to $-0.25\ V$ and measure one final CV in the potential window $-0.25\ V < E < +0.50\ V$ at scan rate $\nu = 50\ mV \cdot s^{-1}$ (the characterization CV). Extending the lower boundary will generally result in the {111} feature diminishing slightly in intensity, but will allow for the presence of the full {100} OH-adsorption feature.

Due to irreversible changes occurring at the upper potential limit, reannealing the surface after characterization is advised. The surface after reannealing will be identical to the surface that was characterized just prior to annealing. Alternatively, one can either halt at step b) and use that surface for the next experiment without the need for reannealing or decrease the upper potential limit in step c) to $+0.44\ V$ and continue without the need for reannealing.

C.1.3. Cu(110) characterization

Contrary to Cu(100) and Cu(111) surfaces, the Cu(110) surface is found to be unstable under the typical surface treatment employed in this work. Specifically, it is found that annealing (and, more importantly, cooling) in pure hydrogen atmosphere results in a (presumably) reconstructed surface with a strongly suppressed {110}-terrace feature (around $+0.33\ V$). Changing the annealing and/or cooling atmosphere to be a mix of argon and hydrogen (of several different compositions) was found to always result in a surface with unstable and/or strongly suppressed {110}-specific OH adsorption feature. Hence, a special electrochemical treatment (step b) was introduced to obtain literature- representative CVs. The following methodology should result in clean, stable and reproducible Cu(110) CVs.

a. Establish initial electrochemical contact at open circuit (E_{oc}).

b. Apply a potential of $-10\ V$ vs. RHE for $30\ seconds$ whilst bubbling argon through the solution (exact cathodic potential not important, so long as it results in large amounts of cathodic current – i.e., several $hundreds$ of $mA \cdot cm_{geo}^{-2}$).

c. This step is a combination of a number of actions:

   c.1. Lift the electrode and break contact with the electrolyte (and stop controlling the potential). Purge the solution with argon for a few minutes to remove the hydrogen and oxygen produced in step b). Every now and again, make and break the meniscus (keeping the electrode at open circuit) to remove dissolved gases in the droplet attached to the surface of the crystal.

   c.2. Change the argon flow to blanket the solution, re-establish meniscus at open circuit.

   c.3. Run a linear sweep from E_{oc} to $0\ V$.

   c.4. Pre-cycle the crystal in the potential window $0\ V < E < +0.3\ V$ for a few cycles (ca. $2-3$). Determine if the CV quickly becomes symmetrical around x-axis. If the CV becomes symmetrical and stable, go to next step. If there is still oxygen (indicated by a lack of symmetry), go back to step c1). Often, repeating step c) in full is necessary for $2-3$ times.

d. Extend the lower CV boundary from $0\ V to -0.25\ V$, and measure one final CV in the potential window $-0.25\ V < E < +0.50\ V$ at scan rate $\nu = 50\ mV \cdot s^{-1}$ (the characterization CV).

Considering that preparing this surface is more intricate than the other surfaces described, it is not advised to reanneal the surface after characterization. Instead, one can rinse the electrode (preferably under hydrogen atmosphere), dry the top of the electrode with a piece of paper (in the case of a disk), and transfer to a working cell to conduct experiments. The {110} facet seems more resistant to oxidation than the other faces, and the cycling up to $+0.50\ V$ does not seem to lead to irreversible oxidation (so long as it is for brief periods). If the rinsing and transfer periods are sufficiently short ($< 1\ min$), reproducible CVs can be obtained via this method.

C.2. Mechanically polished single crystals cleaning procedure

To remove any residues related to the mechanical polishing process, cut single crystals (as-received from the supplier) were treated as described below. This cleaning was found to be necessary, considering that as-received crystals exhibited additional features in the CV unrelated to the adsorption peaks expected for surfaces

of their orientation. It is important to note that the cleaning procedure described below is destructive in nature, and will introduce additional defects into the surface.

Initially the electropolishing methodology as described by Schouten *et al.*[3] and Engstfeld *et al.*[11] was employed in this work for cleaning copper single crystals as per step a). However, this methodology was found to be too aggressive and later on we switched to a milder electropolishing method described by Sebastián-Pascual *et al.*[9, 10, 12] (alternative a). It is strongly advised to employ this alternative electropolishing step (if electropolishing is required), considering that it yields similarly clean surfaces but introduces fewer step-site defects.

The exact cleaning methodology was as follows.

a. The crystal is electropolished by subjecting the electrode to $+2\ V$ vs. a copper CE in $66\ wt\%$ H_3PO_4 solution for $10\ seconds$, followed by $30\ seconds$ at $0\ V$.

(Milder alternative:)

a. The crystal is electropolished at $+1.8\ V$ vs. a Cu CE for $5\ seconds$ in a $10 : 2 : 2\ vol\%$ electrolyte of $H_2SO_4 : H_3PO_4 : H_2O$ which was freshly prepared at the start of the day (hygroscopic action increases the water content over time and results in increased currents at similar potentials, leading to more step defects being generated). Expected (peak) currents during electropolishing: ca. $+300 - 400\ mA \cdot cm_{geo}^{-2}$

b. The crystal is then thoroughly rinsed with Milli-Q water and ultrasonicated in a clean water bath for ca. $10\ minutes$ without being in contact with the sides or bottom of the container.

c. The crystal was thoroughly rinsed with Milli-Q water again, and inductively annealed close to the melting temperature of the material for ca. $5\ minutes$ under H_2 flow, after which it was quench-cooled down to room temperature in increased H_2 flow for another ca. $5\ min$. After taking out the electrode from the annealing compartment, the color should not change as a color change indicates oxide formation (i.e., the crystal has not cooled down sufficiently).

d. Steps a-c) were repeated a minimum of $5\ times$.

Finally, the crystal was electropolished once more (i.e., step a) after which it was thoroughly rinsed and annealed for ca. $15\ min$ (i.e., step c, but for longer). It is then cooled in hydrogen atmosphere, and subsequently electrochemically characterized to ascertain the quality of the surface. In this work, these steps were sufficient to yield surfaces that showed features comparable to what is reported in literature, and thus no additional actions were undertaken.

C.3. Procedure for recovery of defective cut single crystals

Depending on the situation, it is possible that the CV obtained after an experiment does not match that of a clean, well-defined surface. In such instances, two approaches were employed to recover the initial surface structure. As a first option,

the crystal would be inductively annealed as described in the surface preparation section, and then electrochemically characterized to determine if this was sufficient to recover the surface. If the crystal was found to change in the right direction but not fully recover, a longer annealing period was conducted (ca. $15 - 30\ minutes$) and the crystal characterized again.

However, at times, annealing (multiple times, and/or for longer periods) was not sufficient to recover the defective crystal to its initial state. In such cases, the same methodology as described for cleaning mechanically polished surfaces was employed, but steps a-c) were only conducted once (i.e., skipping step d), followed by a long (ca. $15\ min$) annealing step. Then the surface was cooled in a stream of H_2 and electrochemically characterized to verify its structural integrity. This second methodology was repeated until a good surface was obtained, but generally in this work a single treatment was sufficient.

C.4. EASA determination from OH adsorption for Cu(poly) electrodes

To facilitate easier comparison between literature-reported CVs and/or catalytic activities, it is common practice to report data in current density to account for surface area effects. In the case of copper, authors often normalize their data via the geometric area of their surface. However, this form of normalization relies on the inherent assumption that the surface itself is perfectly flat – i.e., has a roughness factor (R_f = 'real area'/geometrical area) of 1. More often than not, this assumption is invalid. To this end, it has been proposed that it is more accurate to determine the so-called electrochemically active surface area (EASA), so as to better represent the actual number of electrochemically addressable sites present at the interface and normalize data using this value.

In this regard, a methodology much employed in the literature for determining this EASA area for copper electrodes is via the double-layer capacity.[13, 14] Briefly, by scanning a small potential window considered purely capacitive in nature at different scan rates, one can determine the total surface capacitance (denoted here C_{tot}, in $Farad$) as the slope by plotting the double layer current (A) as a function of scan rate ($V \cdot s^{-1}$), see Equation C.1.

$$i_{DL}(A) = C_{tot}(F) * \frac{\delta E}{\delta t}(\frac{V}{s}), \text{ where } C_{tot}(F) = C_{DL}(\frac{F}{A}) * A_{Electrochemical} \quad \text{(C.1)}$$

Then, by comparing the total capacitance to a reference value (C_{DL}, labeled C* by Trasatti and Petrii[14]), we can theoretically determine the EASA as per Equation C.2.

$$A_{Electrochemical} = C_{tot}(F)/C_{DL}(\frac{F}{A}) \quad \text{(C.2)}$$

Although this methodology indeed provides an estimate of the number of electrochemically addressable surface sites, it requires the existence of a potential window where purely capacitive behavior is observed, and its accuracy depends

strongly on the availability and validity of a reference capacitance value for the system under consideration (which may vary with the type of electrolyte, and/or the potential window wherein it is measured). In literature, researchers tend to use capacitive surface area measurements via two alternate strategies. Firstly, some measure the total capacitance of their system as per Equation C.1 and determine the area using a literature reference value for C_{DL}. This literature value is generally taken to be $28\ \mu F \cdot cm^{-2}$ (though sometimes reported[15, 16] as $29\ \mu F \cdot cm^{-2}$) in $0.1\ M$ $HClO_4$ for polycrystalline copper as per a publication from 1995 wherein they generalize the capacitance determined for platinum and gold to copper, citing the *'…apparent independence of the capacitance value of the metal'*.[17] Additionally, there are those whom determine their own reference value by measuring the total capacitance of a finely polished surface of known geometric area and assumed surface roughness factor of 1, where they obtain C_{DL} by dividing their obtained C_{tot} by the geometrical area of their surface. Theoretically, these two methods should yield fairly similar (or rather, identical) results, considering they describe the same thing. However, they generally do not, as is illustrated in Table C.1, which summarizes a (by no means exhaustive) number of publications that determined (and used instead) their own reference capacity value for copper under various conditions (original capacitance source included).

From Table C.1, we can clearly see that that there is a rather large spread for the reported reference capacitance, even when it is measured in the same electrolyte ($28 - 78\ \mu F \cdot cm^{-2}$). The differences become even more striking when comparing between differing electrolytes ($4 - 264\ \mu F \cdot cm^{-2}$), showing not only the importance of having a reliable reference in the system under consideration, but also the apparent inaccuracies associated with double layer capacitance surface area determination.[18] In part, these inaccuracies are the result of defining a certain substrate as having a R_f value of 1, which is generally not thoroughly verified (and is difficult to verify for copper, as oxidation/reduction cycles may change the roughness). Additionally, further variability can be related to (differences in) the facet distribution at the interface for surfaces prepared by different groups as some facets are more open than others, resulting in differing capacitance values for differing faces with the total capacitance being the summation of the capacitances of the various sites that make up the surface.

Because of these reasons, researchers investigating non-copper systems generally use other means of determining the real surface area, with electrochemical surface titration-types of methods being popular. Examples include hydrogen and oxygen adsorption studies (e.g., H_{upd} on Pt[19] and surface oxidation of Au[20]), or the deposition of a monolayer of a foreign metal through underpotential deposition (UDP)[14, 21], where the former is more common than the latter.[14, 18] Such electrochemical titration studies are also possible for copper systems, considering that copper is known to yield well-separated adsorption features in hydroxide solution[1, 22, 23], where it is reported that the charge of specific features in the CV can be associated to the geometric areas of particular facets.[23]

Table C.1: Various literature-reported values for C_{DL} as measured in differing laboratories and (possibly) under different conditions /electrolytes.

Reported C_{tot} (μF)	**Reported area (cm^2)**	**Capacitance C_{DL} ($\frac{\mu F}{cm^2}$)**	**Electrolyte**	**Scan rates ($mV \cdot s^{-1}$)**	**Surface**	**Ref**
4	$\pi * 0.52 = 0.785$	5.1	CO_2-saturated 0.1 M $KHCO_3$	Not reported, nor available from cited sources	Cu(100)	[24]
n/a	n/a	16	CO_2-saturated 0.1 M $CsHCO_3$	Not reported, nor available from cited sources	Cu_2O thin film	[25]
n/a	n/a	28	0.1 M $HClO_4$	20, 50, 100, 200, 500	Pt and Au "platinum and gold electrode"	[17]
51	1.13	45.1	0.1 M $HClO_4$	10, 20, 40, 60, 80, 100 (from cited source)	Cu(poly)	[26]
18	$\pi * 0.32 = 0.283$	63.7	1 M NaOH	"...10 to 80"	Cu(poly)	[27]
n/a	n/a	78	0.1 M $HClO_4$	10, 20, 40, 60, 80, 100	Cu(poly)	[28]
n/a	n/a	264	0.1 M KOH	5, 10, 20, 50, 100	Cu(poly)	[29]

With this information in mind, we decided to attempt as best we could to correlate the current integral of a polycrystalline copper surface to its geometrical area, so as to obtain a reference value by which the EASAs of other copper electrodes can be determined via adsorption studies (instead of by their capacitance values). The exact methodology for this process is described in the following section, where we also try to specify all of the assumptions that we must necessarily make for enabling us to determine such a reference adsorption charge density value.

Firstly, we require a clean and flat polycrystalline surface for which we can consistently and accurately expose a known geometrical area to the electrolyte solution. To this end, we opted for preparing a spherical polycrystalline electrode (i.e., droplet at the end of a wire), which we then polished down to about half-way the bead with silicon carbide sandpaper (Hermes, 2500 grid) to yield a bead-type electrode (i.e., a half-sphere at the end of a wire) which was further mechanically polished with diamond slurries (Buehler) of successively smaller sizes from $5\ \mu m$ down to $1\ \mu m$ to yield a mirror finish. Cleaning of the initial spherical droplet was done as per

the methodology described elsewhere in this work (briefly, through a number of iterations of: melting of the bead followed by HNO_3 etching and rinsing with Milli-Q water). Further surface cleaning after mechanical polishing was also performed as described elsewhere in this work (briefly, through a number of iterations of: sonicating the electrode in Milli-Q water for ca. $15\ min$, followed by electropolishing, then rinsing with Milli-Q water and induction annealing in inert atmosphere for ca. $5\ min$).

Considering that the 2D geometry of the resulting surface is determined by the polishing angle with respect to the surface normal of the initial spherical bead (ranging from a perfect circle to oval, depending on the angle), the resulting surface was photographed and the resulting image analyzed to correlate the pixel count of the surface to the area of an item of known dimensions to determine geometric surface area as a more accurate representation of the area as opposed to measuring the diameter and calculating the geometric area by assuming the electrode is perfectly circular. This geometrical area was found to be $0.11\ cm^2_{geo}$.

At this point, we make two assumptions in order to continue our investigation:

(1) The cleaning has led to the successful removal of all surface impurities and/or any contaminants still present on the surface do not contribute to the charge of the CV nor do they block copper surface sites.

(2) The resulting surface is atomically flat (i.e., we define it as having a R_f of 1).

As for the validity of these assumptions, no foreign adsorption features are observed during cyclic voltammetry which would signify the presence of contaminants, which gives credence to assumption (1). Regarding assumption (2), the mechanical polishing and especially electropolishing steps introduce roughness, but this roughness is reduced by the induction annealing step. Still, it is unlikely that the surface is fully atomically flat, but we will have to make this assumption nonetheless.

At this point, we had to decide in what potential window we should determine the charges associated with electro-sorption processes. We opted for measuring in the potential window $-0.25\ V < E < +0.44\ V$, considering that we found that this window exhibits reversible features which is indicative of fast and, importantly, non-destructive adsorption phenomena, whilst encompassing facet-specific adsorption features for all of the basal planes and (likely, see main text) defect sites. This empirical upper potential limit agrees well with the most cathodic tabulated oxidation reaction of copper (Reaction R1).[30] Further indication of the non-destructive nature of the processes occurring in this window is in the form of dissolution studies, wherein it is reported that no copper is detected in solution for potentials $E < 0.5\ V$ vs. RHE during cyclic voltammetry in $0.05\ M$ KOH.[31] The cyclic voltammogram in this window, as obtained for the surface discussed throughout this section, is depicted in Figure C.3.

$$Cu_2O + H_2O + 2\,e^- \rightleftharpoons 2\,Cu + 2\,OH^-, E^0 = +0.41\ V \text{ vs. RHE } (pH13) \quad \text{(R1)}$$

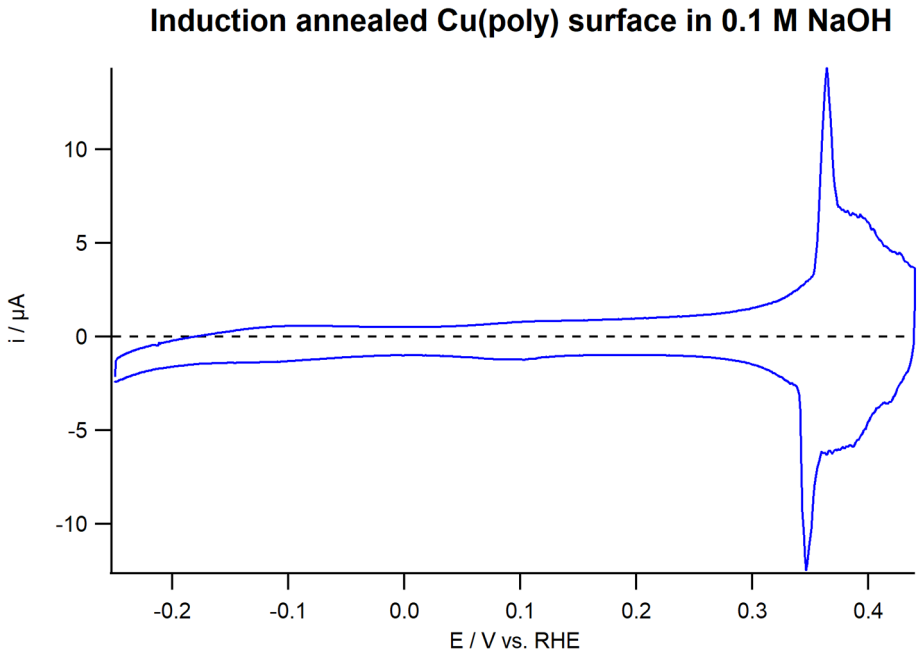

Figure C.3: CV of a mechanically polished and thoroughly cleaned, inductively annealed polycrystalline copper bead-type electrode in $0.1\ M$ NaOH (scan rate $\nu = 50\ mV \cdot s^{-1}$) in the window exhibiting reversible adsorption/desorption behavior.

Though this CV (Figure C.3) is adequate in the sense that it exhibits only features that are related to adsorption phenomena involving copper sites, with clear indication of the presence of a number of different surface sites, it has a minor issue: there is a slight contribution of ORR current at the cathodic end of the CV ($E < +0.1\ V$). This parasitic current contribution was found to be virtually impossible to remove. Although we tentatively ascribe this current to ORR (considering already the region at ca. $0\ V$ is not symmetrical around the x-axis), it may also be related to increased HER on defect sites, or possibly a combination of both.

In order to be able to continue our investigation from this point, we make two additional assumptions:

(3) The adsorption processes occurring on the surface are fully reversible in the potential window that we investigate.

(4) The oxygen concentration in the system is constant, resulting in equal contributions of ORR current at a given potential in both the positive going scan and the negative going scan.

Both assumptions are relatively 'safe', considering that the CV looks symmetrical (providing validity to assumption (3)) and considering that multiple successive scans

result in the same CV (not depicted) without the ORR current contribution changing for either scan direction (leading to assumption (4)).

Under these conditions, the charge contributions of the CV can be divided as follows.

$$\text{Positive going scan: } Q^{f}_{total} = Q^{+}_{adsorption} + Q^{+}_{DL} + Q^{-}_{ORR} \tag{C.3}$$

$$\text{Negative going scan: } Q^{b}_{total} = Q^{-}_{desorption} + Q^{-}_{DL} + Q^{-}_{ORR} \tag{C.4}$$

where Q^{+} denotes an anodic current integral and Q^{-} denotes a cathodic current integral. Additionally, from the assumption that the adsorption processes are fully reversible we can state: $Q^{+}_{adsorption} = -Q^{-}_{desorption}$, and similar reasoning applies to the double layer charge since the scan boundaries are equal for the positive- and negative-going scans: $Q^{+}_{DL} = -Q^{-}_{DL}$. If we now subtract the total charge of the negative-going scan (Q^{b}_{total}) from the total charge of the positive-going scan (Q^{f}_{total}), the ORR contribution cancels out, see Equation C.5. Please note that it is irrelevant if the parasitic (faradaic) current contribution is related to ORR or HER (or a combination of both): so-long as the charge contribution(s) is (are) equal during both scan-directions, they cancel out.

$$\begin{aligned} Q^{f}_{total} - Q^{b}_{total} &= (Q^{+}_{adsorption} + Q^{+}_{DL} + Q^{-}_{ORR}) - (Q^{-}_{desorption} + Q^{-}_{DL} + Q^{-}_{ORR}) \\ &= (Q^{+}_{adsorption} + Q^{+}_{DL} + Q^{-}_{ORR}) + (Q^{+}_{adsorption} + Q^{+}_{DL} - Q^{-}_{ORR}) \\ &= 2 * (Q^{+}_{adsorption} + Q^{+}_{DL}) \end{aligned} \tag{C.5}$$

Now, if we can determine what the double-layer capacity is for our system we could calculate Q^{+}_{DL} and thereby work out the total adsorption-related charge contribution to our CV. We found empirically that the current in the area of the CV between $-0.250\ V < E < -0.235\ V$ was a decent descriptor of surface area; indicative that this area is mostly dictated by capacitive behavior, and therefore we used this region to calculate the double-layer charging current via Equation C.6.

$$i_{DL} = \frac{1}{2} * \left\{ \frac{1}{n} * \sum_{1}^{n} i^{f}(E_n) - \frac{1}{m} * \sum_{1}^{m} i^{b}(E_m) \right\} \tag{C.6}$$

Here, n and m signify the total number of individual datapoints of the CV in the previously defined potential window for the positive-going scan direction and negative-going scan direction, respectively, and $i^{f}(E_n)$ and $i^{b}(E_m)$ denote the currents at the individual potentials associated with datapoints n and m, respectively. For this equation to be valid, we rely once again on assumption (4); that ORR-related faradaic currents cancel out when subtracting the currents for the positive- and negative-going scan directions. The as-calculated value for i_{DL} of the electrode we have been discussing (Figure C.3) was $0.60\ \mu A$ at a scan rate $\nu = 50\ mV \cdot s^{-1}$.

One might argue that it is more accurate to determine (through Equation C.1) the total surface capacitance from scan rate dependency studies of the double-layer

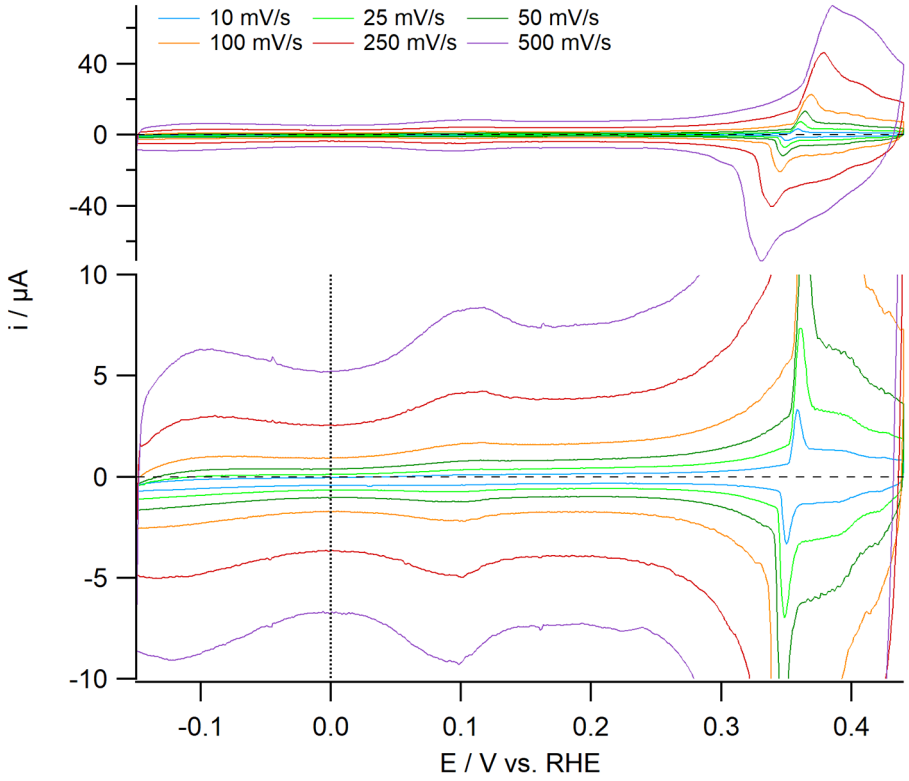

Figure C.4: Scan rate dependency of a polished polycrystalline copper surface in $0.1\ M$ NaOH.

charging current obtained experimentally via Equation C.6, and then back-calculate the theoretical charging current at a particular scan rate from the capacitance. By doing so, besides improved accuracy of the charging current value, one would obtain an additional surface-indicative metric (system capacity, C_{tot}) from basically a single blank CV measurement (just requiring some additional cycling at various scan rates). To briefly address this, we cycled our electrode in the potential window $-0.15\ V < E < +0.44\ V$ (for the scan rate dependency study we increased the lower CV boundary from $-0.25\ V$ to $-0.15\ V$ since {111} terrace sites are not fully stable below $-0.15\ V$ – see main text) at various scan rates (specifically, $10, 25, 50, 100, 250$ and $500\ mV \cdot s^{-1}$) so-as to be able to determine double-layer currents (i_{DL}) at these scan rates. Please mind that the faster scan rates we employ are only viable for surfaces of low roughness. The CVs obtained under these conditions are depicted in Figure C.4.

From the changes in the voltammetry as a function of scan rate, we determined that the area around $0\ V$ exhibited the most capacitive-like behavior (thinnest double-layer with a reasonably stable current although only in a small window). Therefore, we decided to calculate the i_{DL} at each scan rate in the window $-0.005\ V <$

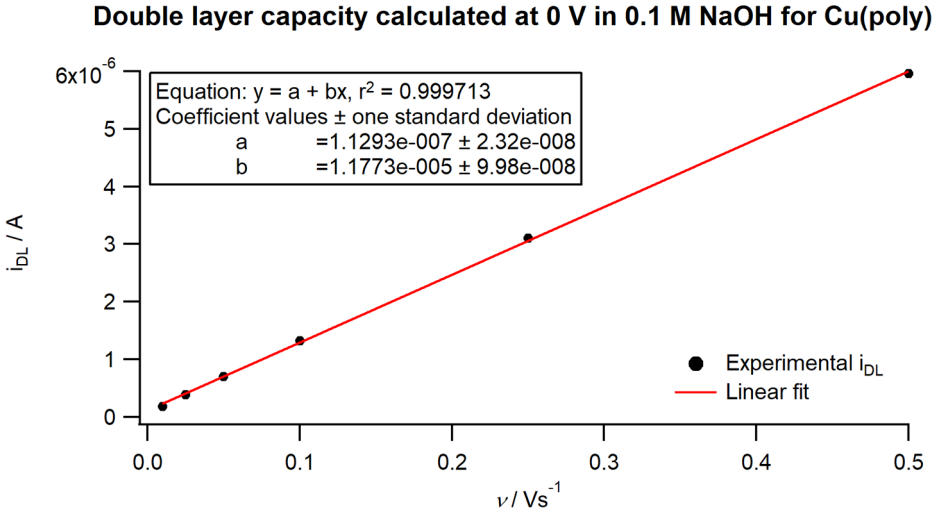

Figure C.5: Total double layer capacity (Ctot) of the polished polycrystalline copper electrode discussed in text, as calculated via Equation C.1 using experimentally determined charging currents as per Equation C.6.

$E < +0.005\ V$ (i.e., $0\ V \pm 5\ mV$) via Equation C.6. However, even though we determined this region seemed most suitable for obtaining the double layer capacity, it must be noted that {100}-terrace sites do yield adsorption-related charge in this window (see main text) albeit a relatively minor amount.

At this point we have the required information for determining the total capacitance, with the results of the linear regression for our flat polycrystalline surface being depicted in Figure C.5. As can be seen from the textbox insert in the figure, the total capacitance we find for our system under our applicable conditions ($0.1\ M$ NaOH, determined at $0\ V$) is $11.77\ \mu F$ (from which we can also calculate the reference capacitance by dividing by the surface area, being $0.11\ cm^2_{geo}$: $C_{DL} = 107\ \mu F \cdot cm^{-2}$). Now we can back-calculate the expected double-layer charging current at a scan rate $\nu = 50\ mV \cdot s^{-1}$ (the scan rate used for the blank CV in Figure C.3) via Equation C.1, yielding $i_{DL} = 0.59\ \mu A$ which is virtually identical to the i_{DL} value we found from our empirically determined DL region of the CV ($-0.250\ V < E < -0.235\ V$, $0.60\ \mu A$). For future calculations, we shall use $i_{DL} = 0.59\ \mu A$, however, in practice, both methods seem suitable for obtaining the double-layer charging current, and both are used in this work depending on the circumstances.

After this brief intermezzo, we now have all the information we require to extract the charge that is due to adsorption processes taking place during the copper CV. Depending on the type of software one uses; it may be easiest to positive-shift the entire CV until all currents are ≥ 0. Then, the positive-going and negative-going scans can be individually integrated, and the latter subtracted from the former, as is visually represented in Figure C.6. For the polycrystalline surface discussed so

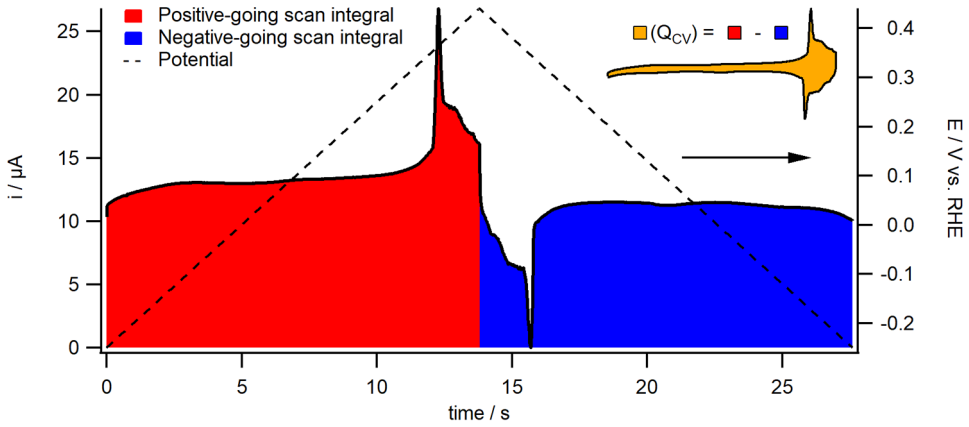

Figure C.6: Visual representation of the charges discussed in text, and what regions they represent.

far in this segment, the charge encompassed by the CV ($Q_{CV} = Q^f_{total} - Q^b_{total}$) was equal to $44.31\ \mu C$.

Finally, we can now determine the area-normalized charge associated with adsorption phenomena on copper via Equation C.7. The part where we multiply the double-layer current by a number of CV parameters is nothing more than the time it takes to finish one full cycle of the voltammogram. The resulting reference charge we obtain find is $128.1\ \mu C \cdot cm^{-2}$.

$$\frac{Q^+_{adsorption}(C)}{A_{geo}(cm^2)} = \frac{1}{A_{geo}(cm^2)} * \frac{1}{2} * \left\{ \left(Q^f_{total}(C) - Q^b_{total}(C) \right) - i_{DL}(A) * 2 * \frac{E_{max}(V) - E_{min}(V)}{scan\ rate \frac{V}{s}} \right\} \tag{C.7}$$

Now, we shall have to make one final assumption in order to use this value for generic EASA determination in our system:

(5) The site distribution of the mechanically polished, subsequently electropolished finally and induction annealed polycrystalline electrode we used to obtain this reference value is representative for all polycrystalline surfaces

The validity of this final assumption is difficult to ascertain. As a first indication, we can deduce if the value we have calculated makes logical sense by comparing our result for polycrystalline copper to literature-reported values for single crystalline surfaces. In this case, Tiwari *et al.*[23] report that the facet-specific adsorption features for {111}, {100} and {110} should theoretically yield adsorption charge densities of respectively $79,\ 59$ and $27\ \mu C \cdot cm^{-2}$. However, the terraces are not

fully covered with OH, having instead the equivalent of between $1/4$ to $1/3$ of a monolayer coverage when considering a Cu:OH ratio of $1:1$ as a full ML. Comparatively, step sites are more reactive than terrace sites, and thus a higher coverage can reasonably be expected for such sites, which happen to make up a significant portion of a polycrystalline surface. Therefore, we believe that the fact that the reference value we obtained for polycrystalline copper ($128.1\ \mu C \cdot cm^{-2}$) is somewhat higher than the range of values reported by Tiwari *et al.*[23] seems reasonable at least.

However, this still does not directly address how applicable assumption (5) is to polycrystalline surfaces of differing site distributions. For now, the best answer to this question is simply to use this methodology of surface normalization, and see how surfaces with different facet distributions compare. To this end, the mechanically polished electrode we have discussed throughout this section is compared to a spherical bead-type polycrystalline electrode (for which it is not possible to readily determine the geometrical surface area) in Figure C.7. From comparing the blue line (polished bead-type electrode) with the red line (spherical bead-type electrode) it is evident that the facet distribution at the interface for these two electrodes is rather different from the fact that they exhibit very different charge contributions in differing regions of the CV. However, after calculating the total adsorption charge for these two surfaces and normalizing the CVs to their respective EASAs, we find that the voltammograms 'look' as one would empirically expect two similarly sized surfaces to behave, though this is decidedly not a convincing argument.Slightly less subjective 'proof' of the normalized CVs representing very similar areas is that the

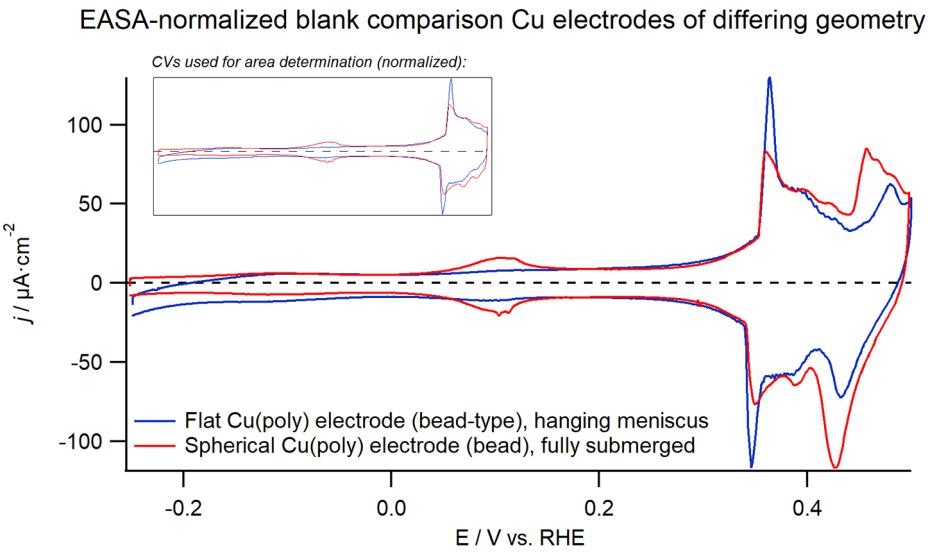

Figure C.7: Two "adsorption EASA-normalized" copper surfaces of strongly different geometry (2D circular vs. 3D spherical) and reasonably different surface-site distribution (as evidenced by the differing intensities at identical potentials in the CVs).

double-layer thickness in the pseudo-capacitive region between $-0.25\ V < E < +0.35\ V$ is very similar between the two surfaces, even though we do not scale directly to this value (it is, however, an integral part of the calculation – as is inherent to surface titration methods).

C.5. Single crystal CV peak deconvolution

C.5.1. Deconvolution of a Cu(111) CV

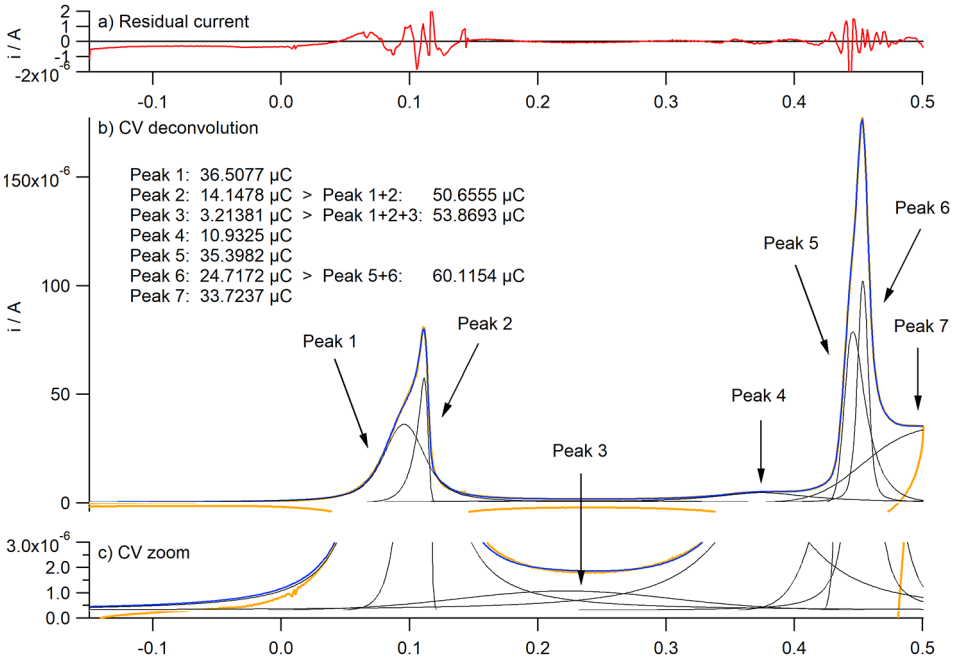

Figure C.8: Mathematical deconvolution of a Cu(111) CV into a sum of individual peaks. In a) the difference in current between the measured CV and the sum of the optimized peaks (red) is given. In b) the locations, shapes and labels of the individual modelled peaks (black) are depicted and compared to the measured CV (orange) and the sum of the optimized peaks (blue). In c) a close-up of b) is given to show the location and shape of peak 3.

In Figure C.8 we have modelled a Cu(111) CV by fitting the observed features to a number of distinct peaks (of varying shapes, e.g., Guassian, Lorentzian, and/or a combination of an Exponential and Gaussian function was used, depending on which fit best the shape of each peak). Considering our belief that {111} terraces with high defect density (i.e., having very narrow widths) yield an adsorption signal at potentials $-0.02\ V < E < +0.25\ V$, we added a representative peak in this region in our deconvolution model (labelled 'peak 3'). Empiric evidence for the existence of this additional peak can derived from the fact that fitting without this peak yields a considerably worse goodness of fit (not depicted). After separating

the individual components, the OH-adsorption charge (sum of the peaks located between $-0.1\ V < E < +0.25\ V$, i.e., peaks 1-3) was estimated to be $53.9\ \mu C$ ($= 107\ \mu C \cdot cm_{geo}^{-1}$), and the adsorption charge associated with the second adsorption feature (sum of the peaks located between $+0.43\ V < E < +0.475\ V$, i.e., peaks 5 & 6) was estimated to be $60.1\ \mu C$, yielding a ratio of ca. $0.9 : 1$. It must be noted that deconvolution of a CV exhibiting such a large number of non-Gaussian features is not very accurate, but can still serve as an indication.

C

C.5.2. Deconvolution of a Cu(100) CV

In Figure C.9 we have modelled a Cu(100) CV by fitting the observed features to a number of distinct peaks. After separating the individual components, the OH-adsorption charge (peak 1, located at $E = -0.125\ V$) was estimated to be $34.5\ \mu C$ ($= 68.7\ \mu C \cdot cm_{geo}^{-1}$), and the charge associated with the second adsorption feature (peak 4, located at $E = 0.475\ V$) was estimated to be $37.9\ \mu C$, yielding a ratio of ca. $0.9 : 1$.

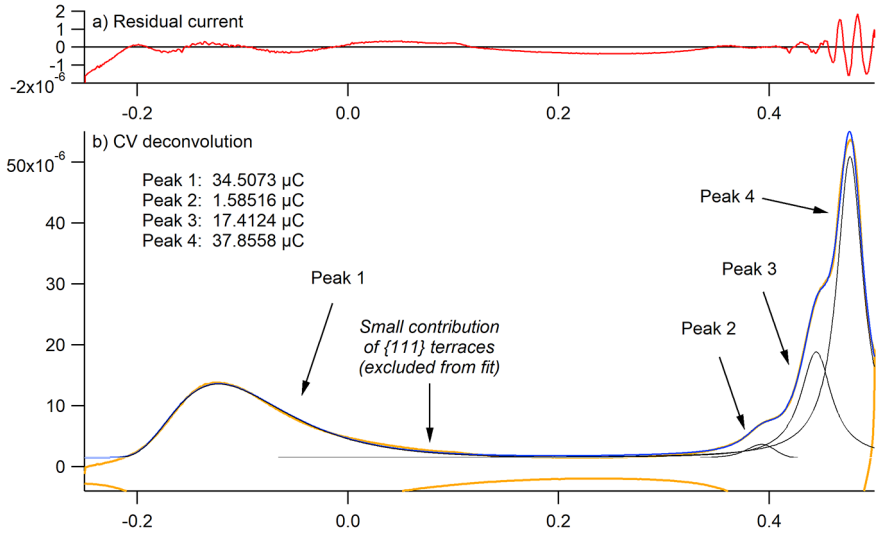

Figure C.9: Mathematical deconvolution of a Cu(100) CV into a sum of individual peaks. In a) the difference in current between the measured CV and the sum of the optimized peaks (red) is given. In b) the locations, shapes and labels of the individual modelled peaks (black) are depicted and compared to the measured CV (orange) and the sum of the optimized peaks (blue).

C.5.3. Deconvolution of a Cu(110) CV

In Figure C.10 we have modelled a Cu(110) CV by fitting the observed features to a number of distinct peaks. After separating the individual components, the OH-adsorption charge (peak 1, located at $E = +0.33\ V$) was estimated to be $13.0\ \mu C$ ($= 25.8\ \mu C \cdot cm_{geo}^{-1}$), and the adsorption charge associated with the second adsorption feature (peak 4, located at $E = +0.494\ V$) was estimated to be $24.5\ \mu C$, yielding a ratio of ca. $1.06 : 2$. Please beware that this CV was found to have the lowest goodness of fit, due a) the cathodic tail of the {110}-specific feature at ca. $+0.33\ V$ which did not conform to any of the typical peak shapes and b) the very broad charge region between $+0.38\ V < E < +0.45\ V$, which is a convolution between several differing sites located close together (i.e., various defect sites and {111} terraces).

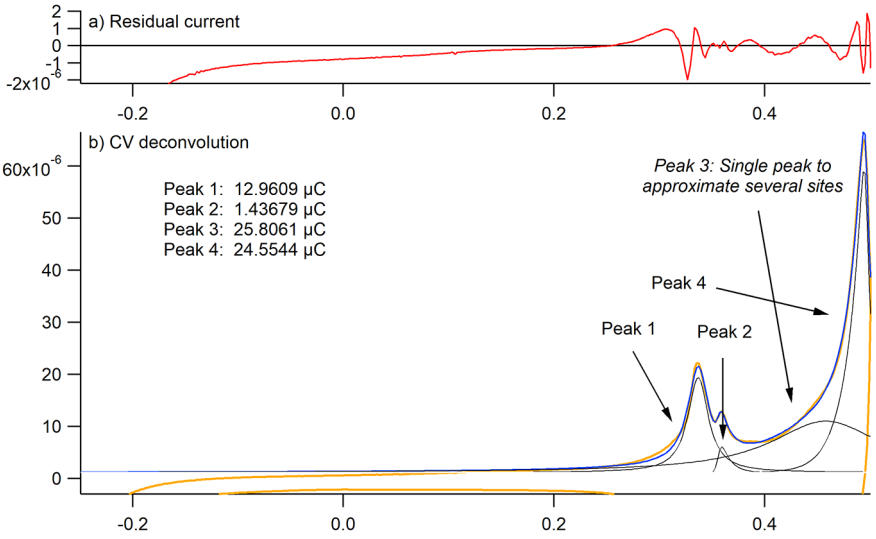

Figure C.10: Mathematical deconvolution of a Cu(110) CV into a sum of individual peaks. In a) the difference in current between the measured CV and the sum of the optimized peaks (red) is given. In b) the locations, shapes and labels of the individual modelled peaks (black) are depicted and compared to the measured CV (orange) and the sum of the optimized peaks (blue).

C

C.6. Preparing clean Cu(poly) with wide site distribution

The following methodology can be used for preparing bead-type polycrystalline copper electrodes. Firstly, one has to prepare a copper bead from a high purity copper wire (ideally $> 99.995\%$ purity) by melting the end of a wire into a droplet via induction heating in inert atmosphere (e.g., H_2, N_2, Ar).

- Re-melt the copper bead, but do not allow it to grow larger (to prevent additional bulk impurities from being introduced to the melt).
- After melting, allow the droplet to cool and solidify in oxygen-free atmosphere by turning off the induction current
- Take out the bead, and etch in concentrated HNO_3 (ca. $5\ seconds$, in a fume hood)
- Rinse the bead with Milli-Q water
- Go back to the first step and repeat procedure (3-5 x)
- After $3-5\ cycles$, remelt the droplet once more, but do not etch again after cooling.

After going through this process, the resulting electrode is ready for experiment after briefly annealing it ($2-5\ minutes$) at ca. $700-800\ ^{\circ}C$ (well below the melting temperature, to prevent further bulk contaminants from migrating to the surface). Working with this type of electrode is slightly more difficult, as it is not possible to make a proper meniscus and thus experimentally challenging to expose the same amount of surface area between different experiments. However, it is possible with some practice. Additionally, small differences in exposed area between experiments can be corrected for by surface area normalization, with electrodes prepared in this way having a near identical facet distribution (and thus CV) when the total area is within $\pm 5\%$ (empirically).

References

[1] Vladimir Jović and Borka Jović. Surface reconstruction during the adsorption/desorption of OH species onto Cu(111) and Cu(100) in 0.1 M NaOH solution. *Journal of the Serbian Chemical Society*, 67(7):531–546, 2002.

[2] Kendra P. Kuhl, Etosha R. Cave, David N. Abram, and Thomas F. Jaramillo. New insights into the electrochemical reduction of carbon dioxide on metallic copper surfaces. *Energy & Environmental Science*, 5(5):7050–7059, 2012.

[3] Klaas Jan P. Schouten, Elena Pérez Gallent, and Marc T.M. Koper. The electrochemical characterization of copper single-crystal electrodes in alkaline media. *Journal of Electroanalytical Chemistry*, 699:6–9, 2013.

[4] Alexander S. Bondarenko, Ifan E. L. Stephens, and Ib Chorkendorff. A cell for the controllable thermal treatment and electrochemical characterisation of single crystal alloy electrodes. *Electrochemistry Communications*, 23:33–36, 2012.

[5] Yongchun Fu, Alexander V. Rudnev, Gustav K. H. Wiberg, and Matthias Arenz. Single graphene layer on Pt(111) creates confined electrochemical environment via selective ion transport. *Angewandte Chemie International Edition*, 56(42):12883–12887, 2017.

[6] V. Komanicky, K.C. Chang, A. Menzel, N.M. Markovic, H. You, X. Wang, and D. Myers. Stability and dissolution of platinum surfaces in perchloric acid. *Journal of the Electrochemical Society*, 153(10):B446, 2006.

[7] Ebru Özer, Benjamin Paul, Camillo Spöri, and Peter Strasser. Coupled inductive annealing-electrochemical setup for controlled preparation and characterization of alloy crystal surface electrodes. *Small Methods*, 3(8):1800232, 2019.

[8] Ebru Özer, Camillo Spöri, Tobias Reier, and Peter Strasser. Iridium(111), iridium(110), and ruthenium(0001) single crystals as model catalysts for the oxygen evolution reaction: Insights into the electrochemical oxide formation and electrocatalytic activity. *ChemCatChem*, 9(4):597–603, 2017.

[9] Sebastián Pascual Paula, Petersen Amanda Schramm, Bagger Alexander, Rossmeisl Jan, and Escudero-Escribano María. *pH and Anion Effects on Cu-Phosphate Interfaces for CO Electroreduction*. 2020.

[10] Paula Sebastián-Pascual and María Escudero-Escribano. Addressing the interfacial properties for CO electroreduction on Cu with cyclic voltammetry. *ACS Energy Letters*, 5(1):130–135, 2020.

[11] Albert K. Engstfeld, Thomas Maagaard, Sebastian Horch, Ib Chorkendorff, and Ifan E. L. Stephens. Polycrystalline and single-crystal Cu electrodes: Influence of experimental conditions on the electrochemical properties in alkaline media. *Chemistry – A European Journal*, 24(67):17743–17755, 2018.

[12] Paula Sebastián-Pascual, Francisco J. Sarabia, Víctor Climent, Juan M. Feliu, and María Escudero-Escribano. Elucidating the structure of the Cu-alkaline electrochemical interface with the laser-induced temperature jump method. *The Journal of Physical Chemistry C*, 2020.

[13] Stephanie Nitopi, Erlend Bertheussen, Soren B. Scott, Xinyan Liu, Albert K. Engstfeld, Sebastian Horch, Brian Seger, Ifan E. L. Stephens, Karen Chan, Christopher Hahn, Jens K. Nørskov, Thomas F. Jaramillo, and Ib Chorkendorff. Progress and perspectives of electrochemical CO2 reduction on copper in aqueous electrolyte. *Chemical Reviews*, 119(12):7610–7672, 2019.

[14] S. Trasatti and O. A. Petrii. Real surface area measurements in electrochemistry. *Journal of Electroanalytical Chemistry*, 327(1):353–376, 1992.

[15] Christina W. Li and Matthew W. Kanan. CO2 reduction at low overpotential on Cu electrodes resulting from the reduction of thick Cu2O films. *Journal of the American Chemical Society*, 134(17):7231–7234, 2012.

[16] Dan Ren, Jinhuan Fong, and Boon Siang Yeo. The effects of currents and potentials on the selectivities of copper toward carbon dioxide electroreduction. *Nature Communications*, 9(1):925, 2018.

[17] P. Waszczuk, P. Zelenay, and J. Sobkowski. Surface interaction of benzoic acid with a copper electrode. *Electrochimica Acta*, 40(11):1717–1721, 1995.

[18] M. Łukaszewski, M. Soszko, and A. Czerwiński. Electrochemical methods of real surface area determination of noble metal electrodes–an overview. *Int. J. Electrochem. Sci*, 11:4442–4469, 2016.

[19] V. Climent and Juan M. Feliu. Thirty years of platinum single crystal electrochemistry. *Journal of Solid State Electrochemistry*, 15(7):1297, 2011.

[20] H. Angerstein-Kozlowska, B. E. Conway, A. Hamelin, and L. Stoicoviciu. Elementary steps of electrochemical oxidation of single-crystal planes of Au—I. chemical basis of processes involving geometry of anions and the electrode surfaces. *Electrochimica Acta*, 31(8):1051–1061, 1986.

[21] Enrique Herrero, Lisa J. Buller, and Héctor D. Abruña. Underpotential deposition at single crystal surfaces of Au, Pt, Ag and other materials. *Chemical Reviews*, 101(7):1897–1930, 2001.

[22] S. M. Abd el Haleem and Badr G. Ateya. Cyclic voltammetry of copper in sodium hydroxide solutions. *Journal of Electroanalytical Chemistry and Interfacial Electrochemistry*, 117(2):309–319, 1981.

[23] Aarti Tiwari, Hendrik H. Heenen, Anton Simon Bjørnlund, Thomas Maagaard, EunAe Cho, Ib Chorkendorff, Henrik H. Kristoffersen, Karen Chan, and Sebastian Horch. Fingerprint voltammograms of copper single crystals under alkaline conditions: A fundamental mechanistic analysis. *Journal of Physical Chemistry Letters*, 11(4):1450–1455, 2020.

[24] Rosa M. Arán-Ais, Fabian Scholten, Sebastian Kunze, Rubén Rizo, and Beatriz Roldan Cuenya. The role of in situ generated morphological motifs and Cu(i) species in C2+ product selectivity during CO2 pulsed electroreduction. *Nature Energy*, 5(4):317–325, 2020.

[25] Anastasia A. Permyakova, Juan Herranz, Mario El Kazzi, Justus S. Diercks, Mauro Povia, Léa Rose Mangani, Michael Horisberger, Alexandra Pătru, and Thomas J. Schmidt. On the oxidation state of Cu2O upon electrochemical CO2 reduction: An XPS study. *ChemPhysChem*, 20(22):3120–3127, 2019.

[26] Youngkook Kwon, Yanwei Lum, Ezra L. Clark, Joel W. Ager, and Alexis T. Bell. CO2 electroreduction with enhanced ethylene and ethanol selectivity by nanostructuring polycrystalline copper. *ChemElectroChem*, 2016.

[27] David Reyter, Marek Odziemkowski, Daniel Bélanger, and Lionel Roué. Electrochemically activated copper electrodes: surface characterization, electrochemical behavior, and properties for the electroreduction of nitrate. *Journal of the Electrochemical Society*, 154(8):K36, 2007.

[28] Alisson H. M. da Silva, Stefan J. Raaijman, Cássia S. Santana, José M. Assaf, Janaina F. Gomes, and Marc T. M. Koper. Electrocatalytic CO2 reduction to C2+ products on Cu and CuxZny electrodes: Effects of chemical composition and surface morphology. *Journal of Electroanalytical Chemistry*, 880:114750, 2021.

[29] Erlend Bertheussen, Arnau Verdaguer-Casadevall, Davide Ravasio, Joseph H. Montoya, Daniel B. Trimarco, Claudie Roy, Sebastian Meier, Jürgen Wendland, Jens K. Nørskov, Ifan E. L. Stephens, and Ib Chorkendorff. Acetaldehyde as an intermediate in the electroreduction of carbon monoxide to ethanol on oxide-derived copper. *Angewandte Chemie International Edition*, 55(4):1450–1454, 2016.

[30] William M. Haynes, David R. Lide, and Thomas J. Bruno. *CRC handbook of chemistry and physics : a ready-reference book of chemical and physical data*. 97 edition, 2017.

[31] Florian D. Speck and Serhiy Cherevko. Electrochemical copper dissolution: A benchmark for stable CO2 reduction on copper electrocatalysts. *Electrochemistry Communications*, 115:106739, 2020.

D

Supporting information for Chapter 5: Morphological stability of copper surfaces under reducing conditions

D.1. Blank reproducibility spherical single crystal

The effectiveness of surface recovery via H_2/ O_2 annealing near the melting point of a copper spherical single crystal after having been oxidized at $+0.70\ V$ for $1\ minute$ is depicted in Figure D.1. In black, the blank as obtained prior to surface oxidation is depicted, and in red the blank obtained after recovering the surface via annealing after it had been oxidized. Comparison of the two blank CVs shows that facet distribution is very similar, although the red line exhibits a larger density of {111} terrace sites as evidenced by increased charge near $+0.1\ V$ (OH-adsorption) and also near $+0.45\ V$ (O-adsorption).

D.2. Anisotropy of halide-induced roughening

Proof of the anisotropic nature of oxidation and reduction of copper in halide-containing solution is provided in Figure D.2, where a SEM image depicting the overall surface of a spherical single crystal post-treatment is provided. Various distinct regions are present on the surface, with their periodicity matching that of the three basal planes in an FCC lattice.

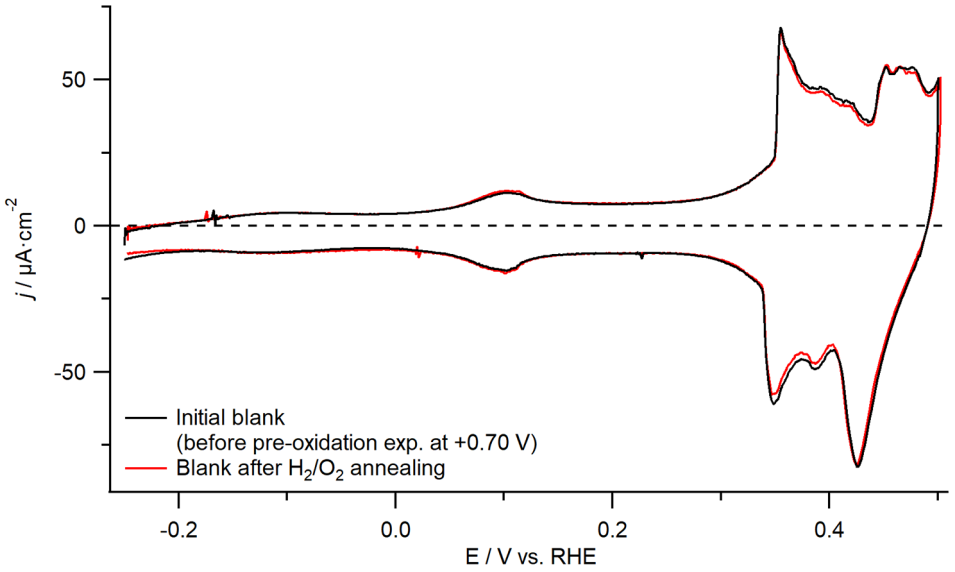

Figure D.1: Blank CV ($0.1\ M$ NaOH, $\nu = 50\ mV \cdots^{-1}$) reproducibility after a pre-oxidation + cathodization experiment ($+0.70\ V / -1.75\ V$, $1\ min$ each) after the crystal was annealed in a H_2 / O_2 flame close to the melting point for $30\ minutes$.

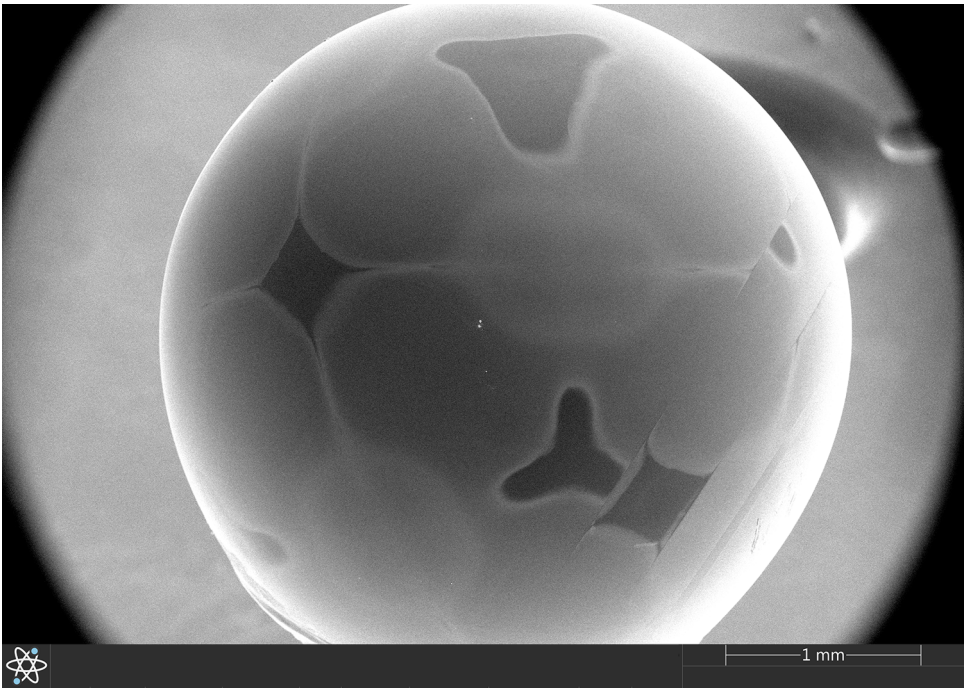

Figure D.2: Blank CV ($0.1\ M$ NaOH, $\nu = 50\ mV \cdots^{-1}$) development for a polycrystalline copper electrode as a function of reaction time during CO2RR at $-0.75\ V$ in $0.1\ M$ $KHCO_3$ electrolyte under continuous CO_2 bubbling. Voltammograms obtained after $1, 5, 15$ and $30\ minutes$ are compared to the initially obtained blank CV in red, green, blue, purple and black, respectively.

D.3. CV evolution after CO2RR in $0.1\ M$ $KHCO_3$

The evolution of the cyclic voltammogram of a copper surface after being subjected to CO2RR at $-0.75\ V$ in $0.1\ M$ $KHCO_3$ for varying amounts of time is depicted in Figure D.3. Clear changes are observed as reaction time is increased, indicated by the arrows in the figure. These changes correspond well with voltammetric changes observed after applying reducing conditions in both $0.5\ M$ $KHCO_3$ and $10\ M$ NaOH (main text).

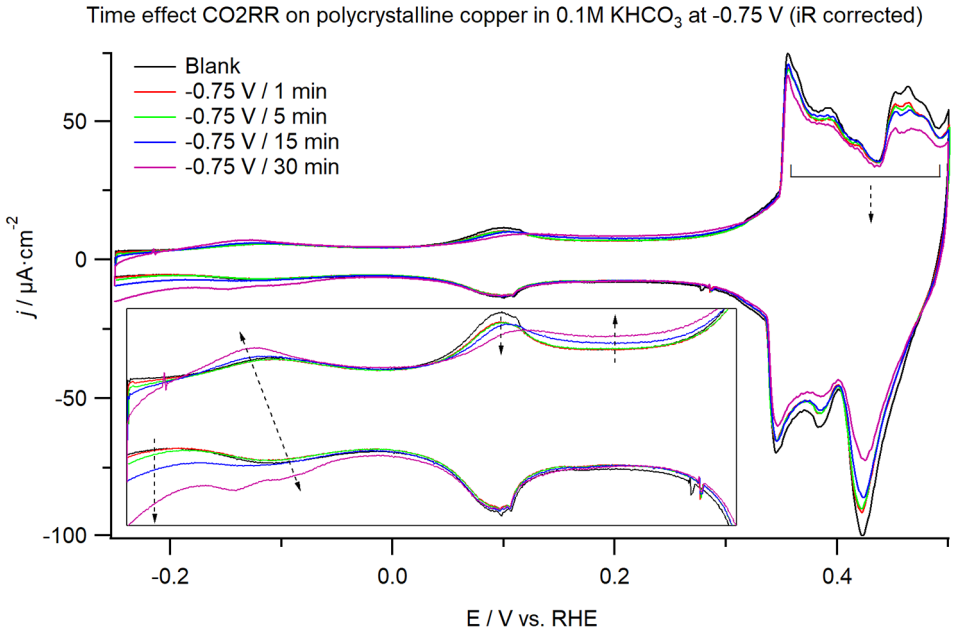

Figure D.3: Surface of a copper spherical single crystal upon anisotropic oxidation and reduction in chloride containing electrolyte (with a grain boundary visible as a result of imperfect crystal growth).

D.4. CV evolution for CORR in $10\ M$ NaOH

Cyclic voltammetry studies were also used to investigate the effect of adding CO during cathodization in $10\ M$ NaOH electrolyte. Furthermore, to guarantee that actual reduction of CO would occur, the applied potential was lowered from $-1.75\ V$ to both $-0.75\ V$ (Figure D.4) and $-0.40\ V$ (Figure D.5). The former potential ($-0.75\ V$) was chosen as it is equal to the potential we used for our CO2RR studies, whereas the latter ($-0.40\ V$) was chosen to see if the presence of CORR intermediates plays a significant role considering that $-0.40\ V$ is close to the onset of the CORR in alkaline media meaning its rate of reduction is much decreased. The changes in voltammetry are virtually identical to what is observed when we apply $-1.75\ V$ in $10\ M$ NaOH without CO present in both cases, though the rate at which the CV changes is somewhat slower in when applying $-0.40\ V$ in the presence of CO.

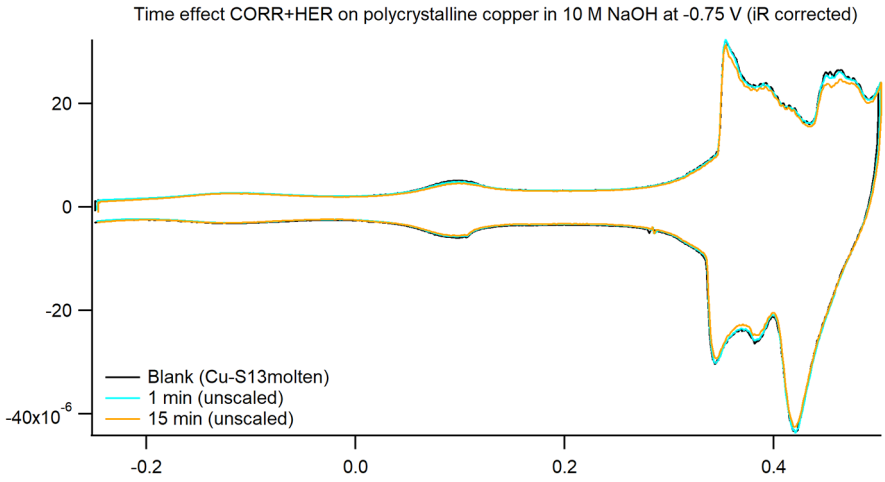

Figure D.4: Blank CV ($0.1\ M$ NaOH, $\nu = 50\ mV \cdots^{-1}$) evolution after conducting CORR experiments in $10\ M$ NaOH electrolyte with active CO bubbling at $-0.75\ V$ for various reaction times.

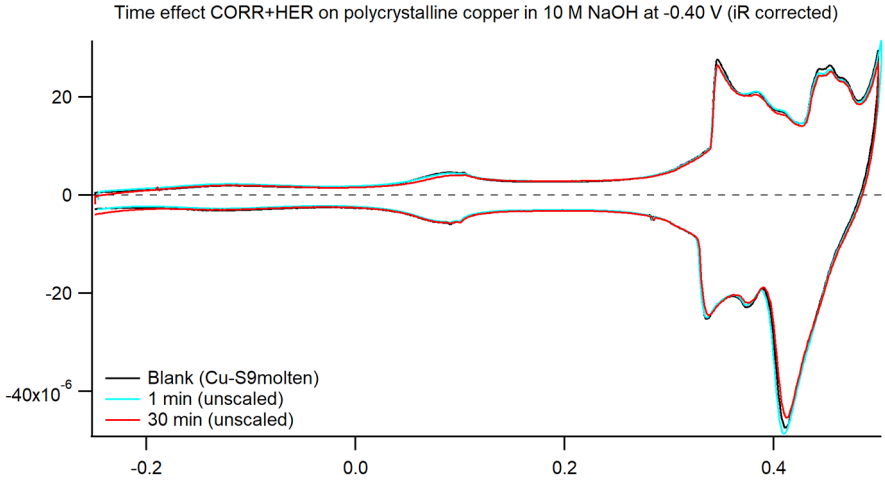

Figure D.5: Blank CV ($0.1\ M$ NaOH, $\nu = 50\ mV \cdots^{-1}$) evolution after conducting CORR experiments in $10\ M$ NaOH electrolyte with active CO bubbling at $-0.40\ V$ for various reaction times.

D.5. Electrode deactivation during CO2RR

Deactivation of the catalytic activity of the roughened spherical single crystal used for SEM studies into the long-term morphological stability of copper under CO2RR conditions ($1\ hour$ at $-0.75\ V$ in $0.5\ M$ $KHCO_3$ electrolyte under constant CO_2 bubbling) is depicted in Figure D.6, in the form of decreasing current response of the system with constant potential.

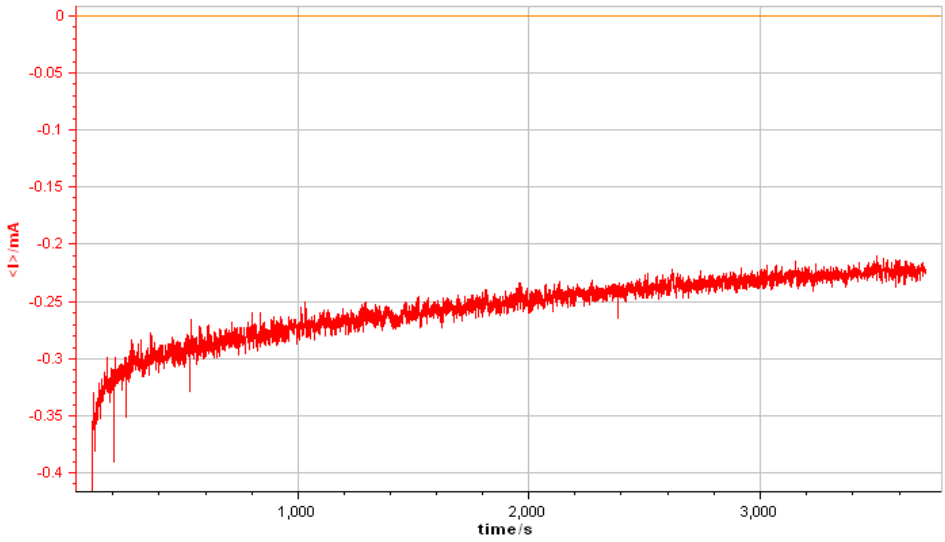

Figure D.6: Time-dependent current deactivation of roughened copper spherical single crystal surface during CO2RR conditions ($-0.75\ V$ in $0.5\ M$ $KHCO_3$ during active CO_2 bubbling).

D.6. Hypothetical morphology-change driven area reduction mechanisms

Assuming that the CV changes discussed in the main text (a decrease in the overall number of active sites, but little change in the relative abundance of the various individual types of sites) are the result of changes in morphology, the following surface restructuring-driven mechanisms can be envisioned.

E.g., one could assume that we start with a rough surface that undergoes considerable restructuring in such a manner that mesoscale and nanoscale deposits change their geometrical shapes towards such geometries that that exhibit lower surface area to volume rations (i.e., spheres). This phenomenon could explain a decrease in overall sites; however, such an explanation is rather unreasonable. Especially when we consider that the electrodes employed in this work are prepared by melting a copper wire into a droplet and allowing it to solidify resulting in a (near) spherical bead which intrinsically has a low roughness factor and low surface area to volume ratio, owing to surface-tension directed surface energy minimization effects.

Another theory that might explain a decrease in area would be to (literally) shrink the electrode radius, and thus decreasing the geometric surface area, via copper dissolution. This explanation is equally unreasonable as the former, considering the large amount of dissolution that would be required. Also, dissolution has been reported to be absent at the negative potentials we employ.[1]

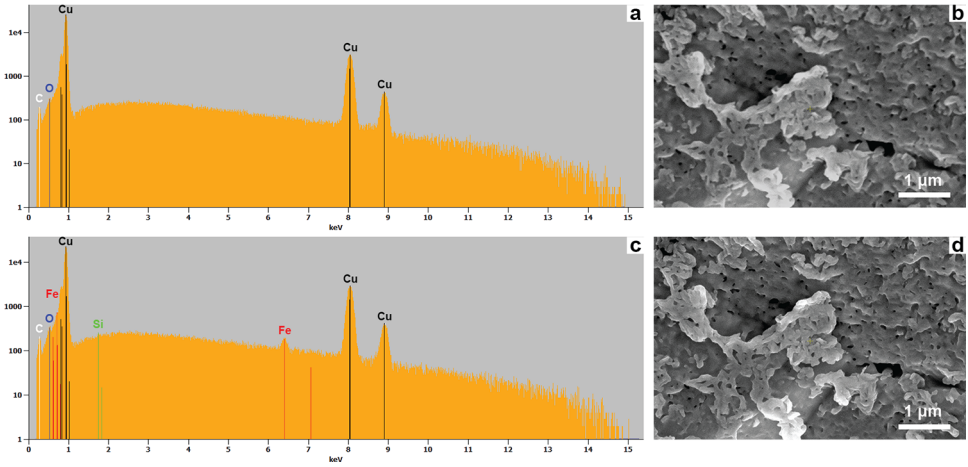

Figure D.7: Surface morphology and elemental analysis results before and after ca. $5\ hours$ of CO2RR at $-0.75\ V$ in saturated $KHCO_3$ solution under constant CO_2 (g) purging for a different location than discussed in the main text with different mesoscopic morphology on a nitric acid-cleaned polycrystalline bead electrode. Panels a and c represent the EDX spectrum a) prior to and c) after CO2RR, whilst b) and d) represent the accompanying SEM micrographs, respectively.

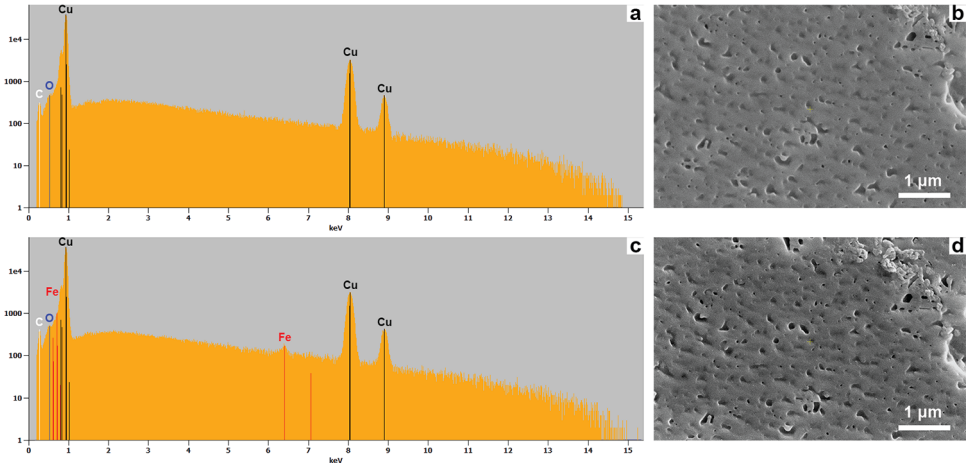

Figure D.8: Equal conditions as Figure D.7, but for a different location on the crystal. Panels a and c represent the EDX spectrum a) prior to and c) after CO2RR, whilst b) and d) represent the accompanying SEM micrographs, respectively.

D.7. EDX study of electrode fouling

Identical-location SEM + EDX experiments were conducted for multiple locations on a nitric acid-cleaned polycrystalline surface as discussed in the main text. Proof that the same observations discussed there hold also for other locations on the crystal is provided in the form of SEM micrographs before and after CO2RR ($-0.75\ V$ in saturated $KHCO_3$ for ca. $5\ hours$) with accompanying EDX signals for two other locations on the crystals in Figures D.7 and D.8.

References

[1] Florian D. Speck and Serhiy Cherevko. Electrochemical copper dissolution: A benchmark for stable CO2 reduction on copper electrocatalysts. *Electrochemistry Communications*, 115:106739, 2020.

Curriculum Vitæ

Stefan was born February 25th, 1991 in Helmond, the Netherlands. After finishing high school, he started a bachelor in chemistry, attending a joint offering by Leiden University and the Delft University of Technology. Choosing to major in courses falling in the domain of expertise of Leiden University and joining the electrochemical laboratory led by prof.dr. Koper for writing his bachelor thesis, he obtained his BSc from Leiden University in 2013. From the same university, after finishing a master thesis based on research conducted in the same laboratory, he obtained his MSc in 2016. Accumulatively, the research conducted during this period resulted in three separate publications.

The culmination of experiences resulted in the opportunity to pursue a PhD in electrochemistry, regarding the (influence of process conditions on the) electroreduction of carbon dioxide, starting 2017. This position was jointly funded by the Dutch Research Council (NWO), the Netherlands Organisation for applied scientific research (TNO) and Shell Global Solutions B.V. The first two years were spent on investigations into cation effects during the electroreduction of CO_2 by metallic copper, including method development of systems to interface gas chromatography and electrochemistry, together with some time allocated to completing teaching duties both as a TA for classes and short-term daily supervision of various (guest) interns. The results of the third through fifth years resulted in the chapters that form the basis of this thesis. Some of the results have been presented at various national and international conferences in the form of posters, with chapters 2 to 5 having been published.

Lastly, during his PhD he also employed vocational schooling as a means of broadening his knowledge by attending the following courses: 'Catalysis: an integrated approach' (2017), 'SurfCat Summer School - The science of sustainable fuels and chemicals' (2018) and 'Photo- and ElectroCatalysis at the Atomic Scale' (2019).

List of Publications

Chapter 2 is based on
Raaijman, S. J., Schellekens, M. P., Corbett, P. J., & Koper, M. T.M. High-Pressure CO Electroreduction at Silver Produces Ethanol and Propanol. *Angew. Chem. Int. Ed.* **2021**, *60* (40), 21732-21736.

Chapter 3 is based on
Raaijman, S. J.[=], Arulmozhi, N.[=], & Koper, M.T.M. Anisotropic Cathodic Corrosion of Gold Electrodes in the Absence and Presence of Carbon Monoxide. *J. Phys. Chem. C.* **2020**, *124* (52), 28539-28554.

Chapter 4 is based on
Raaijman, S. J., Arulmozhi, N., A.H.M da Silva, & Koper, M.T.M. Clean and Reproducible Voltammetry of Copper Single Crystals with Prominent Facet Specific Features Using Induction Annealing. *J. Elec. Soc.* **2021**, *168* (9), 096510

Chapter 5 is based on
Raaijman, S.J.[=], Arulmozhi, N.[=] & Koper, M.T.M. Morphological stability of copper surfaces under reducing conditions. *ACS Appl. Mater. Interfaces* **2021**, *13* (41), 48730–48744

[=] *These authors declare equal authorship*

Other publications

da Silva, A. H., Raaijman, S. J., Santana, C. S., Assaf, J. M., Gomes, J. F., & Koper, M.T.M. Electrocatalytic CO2 reduction to C2+ products on Cu and CuxZny electrodes: Effects of chemical composition and surface morphology. *J. Electroanal. Chem.* **2021**, *880*, 114750

Phan, T. H., Banjac, K., Cometto, F. P., Dattila, F., García-Muelas, R., Raaijman, S. J., Ye, C., Koper, M.T.M., López, N. & Lingenfelder, M. (2021). Emergence of Potential-Controlled Cu-Nanocuboids and Graphene-Covered Cu-Nanocuboids under Operando CO2 Electroreduction. *Nano Lett.* **2021**, *21* (5), 2059–2065

Jacobse, L., Raaijman, S. J. & Koper, M. T. M., The reactivity of platinum microelectrodes. *Phys. Chem. Chem. Phys.* **2016**, *18* (41), 28451-28457.

Diaz-Morales, O., Raaijman, S., Kortlever, R., Kooyman, P. J., Wezendonk, T., Gascon, J., Fu, W. T. & Koper, M. T. M., Iridium-based double perovskites for efficient water oxidation in acid media. *Nat. Commun.* **2016**, *7* (1), 12363.

Kwon, Y., Raaijman, S. J., Koper, M. T. M. Role of peroxide in the catalytic activity of gold for oxidation reactions in aqueous media: an electrochemical study. *ChemCatChem* **2014**, *6* (1), 79–81.

Acknowledgements

This thesis is the eventual and definite conclusion to a journey that I (unbeknownst to me at the time) began the 17th of September, 2012: the day I entered the electrochemical lab of professor Marc Koper to start my bachelor internship under the daily supervision of Youngkook Kwon. At the time I had little knowledge of science and its customs, and although I had the luck of encountering an incredible supervisor, I quickly committed my brief experience with electrochemistry to the past, considering it a dead-end road without future prospects as surely a Bachelor's degree would spell the end of my university career.

The future, however, proved me wrong in my thinking. A rather common occurrence in science, really. Two following internships in electrochemistry, under the care of Oscar Diaz-Morales and Leon Jacobse (my luck with great supervision continued), consolidated both my foundation and interest in electrochemistry. In hindsight, it is these people with their unbridled enthusiasm, patience and positive attitude towards doing science, that gave me courage for making up my mind and crossing the final bridge. To this date, my impressions of my supervisors at the time greatly contribute to my ideology of what constitutes a good scientist. And it seems this is a good location for acknowledging this, thank you for doing science as it should be done, and for guiding me on this path.

Perhaps one might wonder why my supervisor is located all the way in the third paragraph. But there is an order to things, and such an order may as well be chronological. Let the acknowledgement be as follows: there is exactly one laboratory in the world, under the supervision of one specific person, that I would ever have dared to consider my chances of being able to successfully complete a PhD to be anything other than 0%. Paired with my (rather) stubborn personality, it is quite a considerable feat that you a) offered someone like me a position, b) convinced me to actually accept the position, c) allowed me to do science the way I believe it should be done and d) somehow still managed to extract sufficient scientific data out of me to convince others into handing me a title. You are, without a doubt, a good boss to have. And I thank you, for having guided me. However, I am personally more grateful for your continued high quality contributions to the scientific community without losing your way, so to speak. You run a good group, are a good person, and contribute to great science!

And when speaking of a running a good group, I personally believe that José Dijkzeul is one of the secret weapons to keep things operational. I thank you, for all the things you do daily that I know about, and for the many more things that you do that I do not know about. Similarly to Marc, you go above and beyond. And although I may not agree a person should be expected to continually go the extra mile, as so often is, I do fully believe you deserve to be acknowledged for your contribution to the machinery that keeps scientists doing what they (presumably)

do best: science.

The last section I shall keep generic, as who we are is influenced by everything and everyone near to us, in heart and mind or simply in time and space. And who we are, impacts what we do. It is a futile effort to try and quantify such things and therefore I've decided the fairest way is to average it out. Firstly, I shall thank all of my collaborators who have been working together with me, and for this exact reason have already been named as co-authors on the publications that also carry my name. Secondly (and lastly), I'd like to thank family, friends and colleagues (former and current) for being there along the way and making time for coffee, beers, conversations and help, and the occasional bout of shenanigans.